Article

Cavity-mediated thermal control of metal-to-insulator transition in 1T-TaS₂

Giacomo Jarc[1,2], Shahla Yasmin Mathengattil[1,2], Angela Montanaro[1,2,3], Francesca Giusti[1,2], Enrico Maria Rigoni[1,2], Rudi Sergo[2], Francesca Fassioli[3,4], Stephan Winnerl[5], Simone Dal Zilio[6], Dragan Mihailovic[7], Peter Prelovšek[7], Martin Eckstein[8] & Daniele Fausti[1,2,3 ✉]

Placing quantum materials into optical cavities provides a unique platform for controlling quantum cooperative properties of matter, by both weak and strong light–matter coupling[1,2]. Here we report experimental evidence of reversible cavity control of a metal-to-insulator phase transition in a correlated solid-state material. We embed the charge density wave material 1T-TaS₂ into cryogenic tunable terahertz cavities[3] and show that a switch between conductive and insulating behaviours, associated with a large change in the sample temperature, is obtained by mechanically tuning the distance between the cavity mirrors and their alignment. The large thermal modification observed is indicative of a Purcell-like scenario in which the spectral profile of the cavity modifies the energy exchange between the material and the external electromagnetic field. Our findings provide opportunities for controlling the thermodynamics and macroscopic transport properties of quantum materials by engineering their electromagnetic environment.

Optical driving with ultrashort pulses has been extensively used to dynamically control the properties of complex quantum materials[4–9]. Yet, several theoretical proposals indicate that the control of materials functionalities can be obtained by modifying their electromagnetic environment, embedding the materials into optical cavities, even in the absence of a driving field[1,2]. Predictions range from enhanced superconductivity through cavity-mediated electron pairing[10–15], cavity control of the competing order between charge density wave and superconducting phases[16], cavity control of excitons[17], enhanced ferroelectricity[18–20] and cavity control of magnetic orders[21]. Experimentally, it has been demonstrated that vacuum fields in the strong coupling regime[1] can change material functionalities as, for example, the magneto-transport in two-dimensional materials[22], the topological protection of the integer quantum Hall effect[23] or the magnetic order in unconventional superconductors[24].

Cavity control of phase transformations in complex systems can be achieved by distinct physical mechanisms. On the one hand, the selective coupling of the cavity modes to the excitations of a given phase can renormalize its free energy with respect to that of other ones, thereby modifying the temperature at which the phase transition occurs. On the other hand, a cavity can reshape the exchange of energy between a material and the thermal reservoir of photons in which the material is immersed[25]. By engineering the density of states of the electromagnetic environment at the sample position through tunable optical cavities, it is possible to modify the absorption and emission of the sample[26–29] and, in turn, its temperature (T_{int}). Figure 1a shows the two aforementioned cavity-mediated mechanisms.

In this work, we investigate the metal-to-insulator phase transition in the transition metal dichalcogenide 1T-TaS₂ embedded in low-energy terahertz (THz) and sub-THz cryogenic cavities (Fig. 1a). 1T-TaS₂ exhibits a temperature-dependent charge order that originates from the competition of Coulomb repulsion, lattice strain, interlayer hopping and Fermi-surface nesting[30–32]. At ambient temperature, 1T-TaS₂ is in a nearly commensurate charge density wave (NC-CDW) phase with metallic character, featuring hexagonal-shaped polaron domains[30,33,34] forming a David's star pattern[35–37] (Fig. 1c). By lowering the temperature below about 180 K, a transition to an insulating commensurate charge density wave (C-CDW) state occurs[31,38]. We note that the free-energy landscape of 1T-TaS₂ is much more complicated than the simple diagram in Fig. 1a: the phase transitions in 1T-TaS₂ are several and sensitive to the thermal history of the sample. On heating from the C-CDW phase, an additional intermediate trigonal (T) phase with in-plane charge stripes occurs at around 220 K and persists up to around 280 K, when the NC-CDW is re-established[39].

THz spectroscopy is a powerful tool for tracking the metal-to-insulator transition because it can measure contactless the quasi-static dielectric response associated with the presence of conductive charges characteristic of a metallic state (see Methods and ref. 3 for further details on the experimental set-up). Here we use broadband time-domain THz spectroscopy to track the charge order in the sample for different cavity settings. We demonstrate that a bidirectional switch between the metallic and insulating phases can be obtained by tuning the cavity length and adjusting the alignment of its mirrors while keeping the cryogenic temperature of the sample support and mirrors fixed.

A simultaneous measurement of the actual temperature of the sample inside the cavity (T_{int}) and THz transmission is not possible. At a practical level, the placement of a physical thermometer within the

[1]Department of Physics, Università degli Studi di Trieste, Trieste, Italy. [2]Elettra Sincrotrone Trieste, Trieste, Italy. [3]Department of Physics, University of Erlangen-Nürnberg, Erlangen, Germany. [4]International School for Advanced Studies (SISSA), Trieste, Italy. [5]Institute of Ion Beam Physics and Materials Research, Helmholtz-Zentrum Dresden-Rossendorf, Dresden, Germany. [6]CNR-IOM, TASC Laboratory, Trieste, Italy. [7]Jožef Stefan Institute, Ljubljana, Slovenia. [8]Institute of Theoretical Physics, University of Hamburg, Hamburg, Germany. ✉e-mail: daniele.fausti@elettra.eu
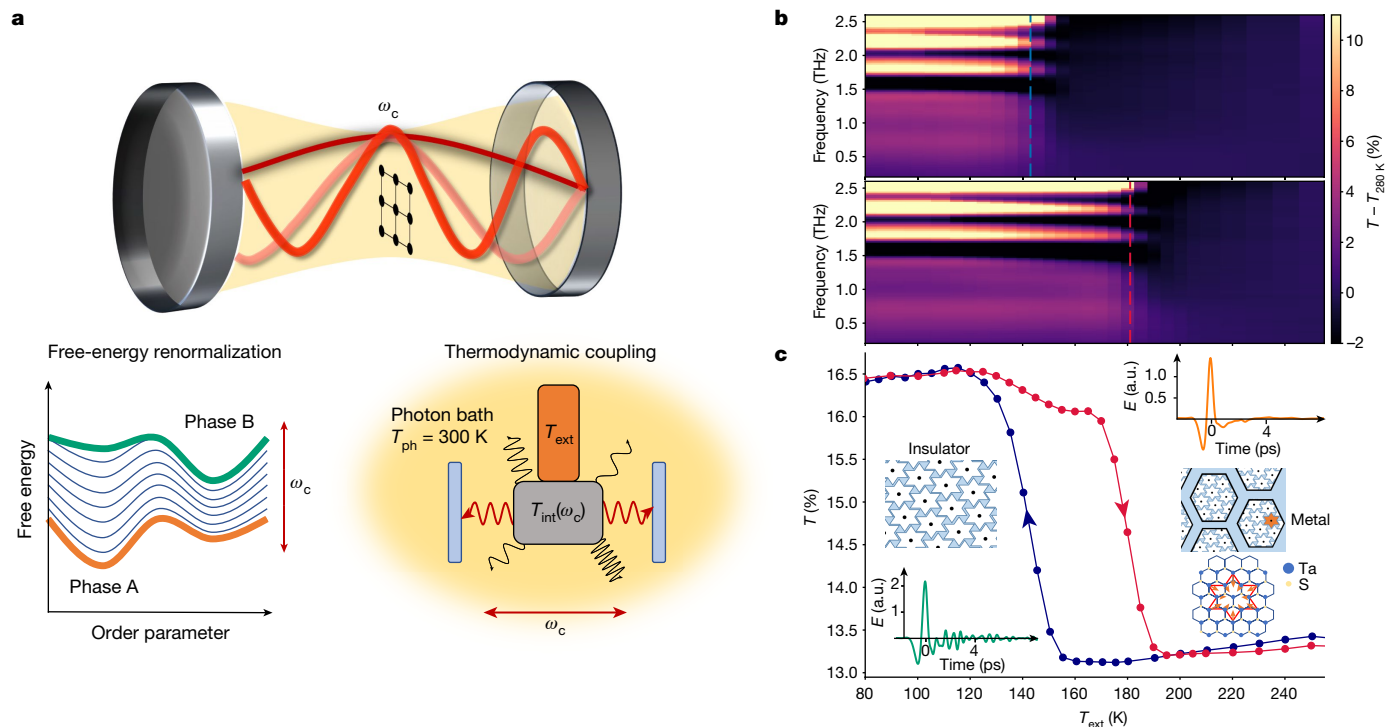
Fig. 1 | Mechanisms of cavity control of quantum material states and THz characterization of 1T-TaS$_2$ metal-to-insulator transition. a, Schematic of a material embedded in the middle of a tunable optical cavity with controllable fundamental frequency ω_c and alignment. Coupling of the excitations of the material with the cavity mode can act on the thermodynamics of the sample in two different scenarios. On the one hand, it can renormalize the free energy of one material phase with respect to the other (bottom left). On the other hand, as a function of ω_c the cavity can reshape the emission and absorption of the material, subsequently rescaling its local temperature $T_{int}(\omega_c)$ with respect to the temperature measured on the sample support (T_{ext}) (bottom right). **b**, THz linear transmission spectra in free space at different temperatures across 1T-TaS$_2$ metal-to-insulator transition (temperature scans performed by cooling (top) and heating (bottom)). To highlight the phase transition, each spectrum has been subtracted from the 280 K THz transmission. **c**, Temperature dependence of the integrated low-frequency transmission (0.2 THz < ω < 1.5 THz), marking the metal-to-insulator transition and its hysteresis. Insets: the time-domain THz fields are shown for the metallic and the insulating phases, together with the illustration of the in-plane lattice modulations characteristic of the insulating C-CDW phase and of the metallic NC-CDW phase. a.u., arbitrary units.

cavity would absorb the THz pulses and make the transmission measurements unfeasible. At a fundamental level, any object placed within the optical cavity will perturb the cavity environment and therefore the response of the light–matter assembly. For this reason, we have designed an experimental protocol in which, for the THz characterization, we measure the temperature on the cold-finger support of the sample outside of the cavity, denoted as T_{ext} (Fig. 1a). This protocol enables us to identify an effective critical temperature T_c^{eff} for the phase transition, which is defined as the temperature of the support at which the phase transition is observed. In a separate measurement campaign, we place a micrometric thermocouple and measure the temperature at the sample position for different experimental configurations (with and without the sample), which we denote as T_{int}, while simultaneously monitoring the external temperature T_{ext}.

THz spectroscopy of 1T-TaS$_2$

Figure 1b shows the THz linear transmission of 1T-TaS$_2$ in free space on heating and cooling as a function of the temperature of the sample support (T_{ext}). This captures the first-order transition between the NC-CDW metallic phase and the C-CDW insulating phase. The phase transition results in (1) an increase in the low-frequency transmission (0.2 THz < ω < 1.5 THz) below the effective critical temperature, which is consistent with a transition to an insulating behaviour (Drude-like response of free carriers vanishes in the insulating phase[40,41]); and (2) the emergence below T_c^{eff} of infrared-active optical phonons at 1.58 THz, 2.04 THz and 2.35 THz, which are screened by the free

carriers and, therefore, not visible in the metallic phase (Fig. 1c, inset, reports time-domain THz traces representative of the two phases). We will use the temperature dependence of the integrated low-frequency transmission (0.2 THz < ω < 1.5 THz) as a marker that tracks the charge-order dynamics in 1T-TaS$_2$ and hence the metal-to-insulator phase transition (Fig. 1c). The low-frequency transmission is directly mapped to the evolution of the Drude optical conductivity $\sigma_1(\omega)$ representative of the free carriers response (Supplementary Information). Analogous transition temperatures can be obtained by tracking the temperature dependence of the transmission at the phonon frequency (Methods). The temperature dependence of the integrated low-frequency transmission (0.2 THz < ω < 1.5 THz) of the material in free space is shown in Fig. 1c. The difference between the results obtained on heating and cooling the sample in free space marks the hysteresis associated with the first-order phase transition. The phase transition in free space occurs at T_{ext} = 181 K on heating and at 143 K on cooling from the metallic phase. Note that the smooth transition observed can be ascribed to the presence of intrinsic inhomogeneities and strain in the system, which may smear out the first-order transition[42–44] (Methods). The effective critical temperature T_c^{eff} measured in our set-up differs from the literature value[31] by about 35 K. This discrepancy is attributed to the difference between the internal temperature of the sample (T_{int}) and the temperature of the cold finger of the cryostat (T_{ext}), as a consequence of the small thermal conductivity of the silicon nitride membranes holding the 1T-TaS$_2$ sample[3]. A finite-elements simulation of the thermal profile of the membrane is in quantitative agreement with the measured temperature shift (Methods).
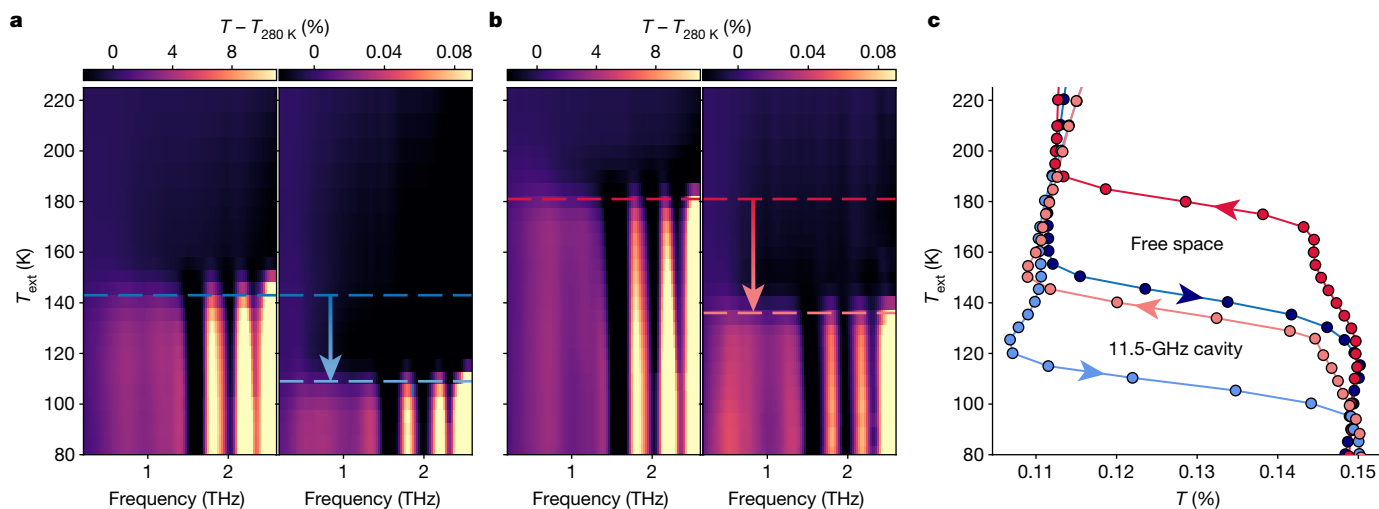
Fig. 2 | Renormalization of the effective critical temperature of the metal-to-insulator phase transition within the cavity. a,b, Temperature-dependent THz transmission on cooling (**a**) and heating (**b**) for a sample held in free space (left) and one placed in the middle of the 11.5-GHz cavity (right). **c**, Comparison of the hysteresis in free space and within the 11.5-GHz cavity plotted as the integrated cavity transmission in the range 0.2 THz < ω < 1.5 THz.

The free-space data have been arbitrarily translated along the horizontal axis to overlap with the cavity-integrated transmission. In the cavity, a renormalization of the effective critical temperature of 44 K towards lower temperatures is measured on heating and 33 K on cooling the sample. This results in a shrinking of the effective phase-transition hysteresis of 11 K within the cavity.

1T-TaS$_2$ characterization in cryogenic THz cavities

Figure 2 shows the THz linear transmission as a function of the sample-holder temperature (cooling in Fig. 2a and heating in Fig. 2b) of 1T-TaS$_2$ in free space and embedded in the centre of an optical cavity with resonant frequency $\omega_c = 11.5$ GHz and quality factor $Q \approx 4$ (Methods). The placement of the sample in this cavity results in a modification of T_c^{eff} for the metal-to-insulator transition, which is observed at 136 K on heating and 109 K on cooling. The modification of T_c^{eff} depends also on the thermal cycle. A change of T_c^{eff} of 44 K is observed if the critical temperature is approached from the insulating state (heating), whereas a shift of 33 K is obtained starting from the metallic phase (cooling), resulting in a shrinking of the hysteresis of about 11 K. We highlight that T_c^{eff} is independent of the input intensity of the THz field, which, therefore, acts only as a probe and does not introduce a detectable thermal load on the sample (see Supplementary Fig. 15 for measurements with different THz field strengths).

Next, we varied the cavity geometry and measured T_c^{eff} as a function of the alignment of the cavity mirrors. We quantify the cavity misalignment as the sum of the misalignment angles of the two cavity mirrors Θ with respect to the configuration of the parallel mirrors. The temperature dependence of the low-frequency THz transmission (0.2 THz < ω < 1.5 THz integration range) at different mirror alignments is shown in Fig. 3a for the temperature scans performed by heating and cooling the cold-finger sample holder. Misaligning the mirrors modifies T_c^{eff}, which approaches the free-space value when the cavity is highly misaligned (Fig. 3a). In Fig. 3a (inset), we show that a switch between the metallic and the dielectric linear response is obtained at fixed T_{ext} by solely changing the cavity alignment. As any misalignment of the cavity mirrors reduces the photon lifetime within the cavity (and hence the quality factor), the sensitivity of T_c^{eff} not only to the presence of the cavity but also to the alignment of the mirrors is suggestive of a cavity-mediated effect. This is further supported by the fact that misaligning the cavity mirrors not only changes the effective critical temperature but also increases the hysteresis of the metal-to-insulator transition towards its free-space value.

Figure 3b reports the THz transmission as a function of the cavity fundamental frequency at a fixed cold-finger temperature ($T_{\text{ext}} = 150$ K). The results indicate that the cavity-mediated change of T_c^{eff} can overcome the free-space hysteresis, thus enabling a reversible touch-less control of the metal-to-insulator phase transition. On reducing the distance between the mirrors, we detected the phase transition between the metallic and the insulating phases to occur at a cavity frequency of 25.0 GHz. This is highlighted in the THz time-domain traces of Fig. 3b (insets) by the screening of the infrared-active phonon modes of the C-CDW insulating phase. After the system had fully switched to the insulating state, we decreased the cavity fundamental frequency and detected a switch to the metallic phase at a lower cavity frequency (13.6 GHz). This results in the cavity frequency-dependent hysteresis highlighted in Fig. 3b.

The detailed dependence of T_c^{eff} on the cavity fundamental mode is presented in Fig. 4a. We measured the effective transition temperature for cavity frequencies ranging from 11.5 GHz to 570 GHz. Importantly, the maximum cavity frequency used lies below the frequency of the lowest infrared-active mode of the C-CDW phase (1.58 THz as shown in Fig. 1c). We made this choice to disentangle possible effects because of the coupling to the infrared-active optical phonons of the CDW.

Figure 4a summarizes the dependence of the measured T_c^{eff} (heating and cooling) on the cavity resonant frequency. The results indicate a non-monotonic trend of T_c^{eff} as a function of cavity resonant frequency with respect to the free-space condition. Whereas long-wavelength cavities (up to about 25 GHz) stabilize the nearly commensurate metallic phase, higher energy cavities effectively favour the insulating C-CDW phase with respect to the material in free space (represented in Fig. 4 as the zero-frequency point). Overall, we showed a shift of 75 K by moving from the lowest energy cavity used in the experiment (11.5 GHz) towards the highest energy cavity (570 GHz).

We note that the value of T_c^{eff} in the cavity with the lowest frequency achievable in our set-up is approximately 30 K below the T_c^{eff} measured in free space (Fig. 4a). This anomalous behaviour cannot be rationalized by incoherent radiation heating because of the presence of the mirrors. Crucially, the exclusion of an incoherent heating mechanism is confirmed by the fact that the dependence of T_c^{eff} on the cavity geometry is qualitatively similar for measurements with cavity mirrors at different temperatures (Supplementary Figs. 4 and 5). This is in contrast with a scenario in which thermal radiation is transmitted incoherently to the sample (incoherent radiation heating), which would give
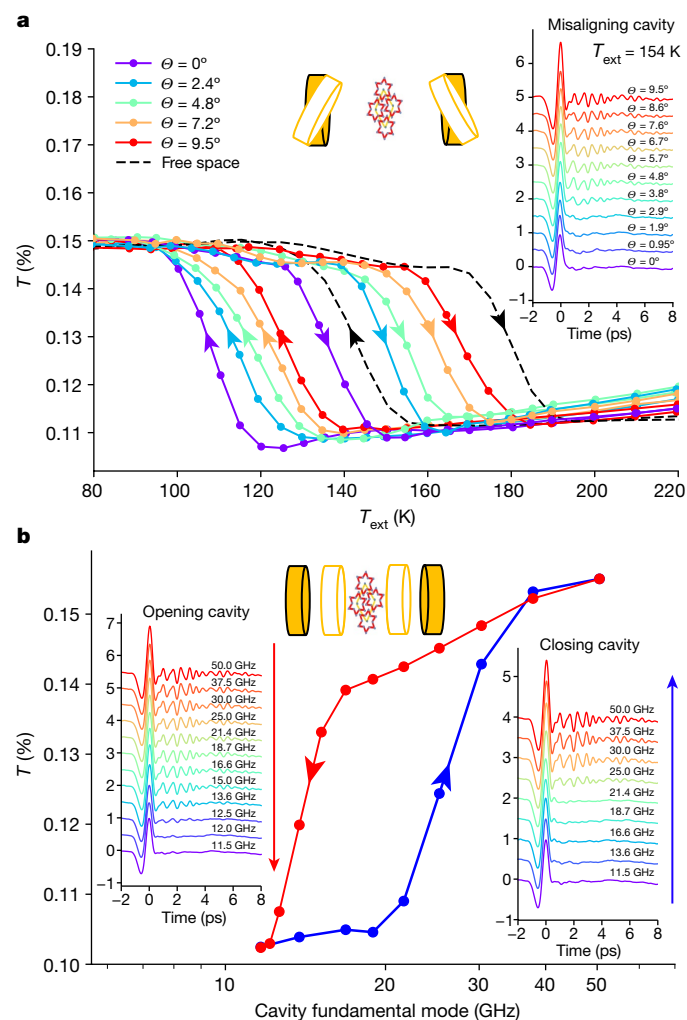
Fig. 3 | Dependence of the effective critical temperature on the cavity geometry. a, Dependence of the metal-to-insulator phase transition as a function of the cavity alignment for the 11.5-GHz cavity. The hysteresis is plotted for each misalignment angle Θ as the integrated low-frequency transmission (0.2 THz < ω < 1.5 THz). Inset; THz fields detected at the output of the coupled 11.5-GHz cavity at a fixed temperature (T_{ext} = 154 K) as a function of the mirror alignments. Transition from the dielectric to the metallic behaviour is detected passing from the misaligned to the aligned configuration. **b**, Reversible cavity control of the metal-to-insulator transition at fixed external temperature (T_{ext} = 150 K). The hysteresis as a function of the cavity fundamental mode is plotted as the evolution of the integrated low-frequency THz transmission (0.2 THz < ω < 1.5 THz). Insets: evolution of the time-domain THz fields transmitted for different values of the cavity frequency ranging from 50.0 GHz to 11.5 GHz (opening cavity case) and from 11.5 GHz to 50.0 GHz (closing cavity case), demonstrating the reversible switching between the two phases.

opposite trends with hot and cold cavity mirrors (see finite-elements simulation of incoherent radiation heating with hot and cold mirrors in Supplementary Figs. 6 and 7 and discussion therein).

Having established that the observed effect cannot be rationalized by incoherent radiation heating, in the following we focus on understanding if the observation could be explained by cavity-mediated heating or cooling or by a free-energy renormalization (the two scenarios presented in the introduction, Fig. 1a). To determine whether the cavity is influencing the temperature at the sample position (that is, inside the cavity), we performed an independent measurement campaign to simultaneously measure T_{int} and T_{ext}. To this purpose, a micrometric custom-designed Cr–Al junction was used (Methods).

Figure 4b shows, for representative cavity frequencies, the difference between the temperature measured within the cavity (T_{int}, in thermal contact with the sample) and the temperature of the cold finger (T_{ext}) as a function of T_{int}. On changing the cavity mode, we showed a non-monotonic trend of the differential temperature $T_{int} - T_{ext}$ with respect to the free-space configuration. Whereas lower frequency cavities induce coherent heating of the sample, the coupling with higher energy cavity modes decreases the temperature of the sample with respect to the free-space conditions. By tracking the T_{ext} at which T_{int} = 210 K (nominal critical temperature of 1T-TaS$_2$), we showed a non-monotonic trend as a function of the cavity frequency (Fig. 4b, inset), which is qualitatively consistent with the observation in Fig. 4a.

There are two important aspects: (1) The observed anomalous non-monotonic trend of $T_{int} - T_{ext}$, as well as its dependence on the cavity frequency, depends on the presence of the sample (the temperature difference is much smaller and monotonic when the thermocouple is mounted within the membranes without the sample) (Supplementary Fig. 1a,b). (2) We repeated the measurements with mirrors at 290 K, revealing, apart from a rigid shift, a trend with cavity frequency analogous to the one observed with cryogenic mirrors (Supplementary Fig. 8). Crucially, a decrease in T_{int} on closing the cavity, regardless of the temperature of the mirrors, is incompatible with an incoherent radiative scenario and points towards a cavity-mediated effect.

In light of the temperature measurements of Fig. 4b, the cavity frequency-dependent hysteresis in Fig. 3b can be rediscussed in terms of an effective renormalization of the sample temperature in the presence of the cavity. By keeping fixed the cold-finger temperature (T_{ext}), the local temperature of the sample (T_{int}) decreases on increasing the cavity frequency (Supplementary Fig. 8). Therefore, closing the cavity effectively corresponds to cooling down the sample that is thus driven to the insulating state (Fig. 3b, blue curve). The effect is reversed when, starting from the insulating state, the cavity frequency is decreased (red curve). Closing and opening the cavity, leading to the hysteretic behaviour in Fig. 3b, can then be interpreted as an effective change in the sample temperature induced by the cavity environment that is different in the two phases. Similarly, the alignment dependence of Fig. 3a can be linked to a mirror-controlled change in the temperature of the cavity-confined material (Supplementary Fig. 9).

Changing the cavity frequency leads not only to a renormalization of T_c^{eff} but also to an effective shrinking of the hysteresis of the phase transition. This is demonstrated in Fig. 4c in which we plot the comparison of the phase-transition hysteresis for a low- and high-frequency cavity (ω_c^{low} = 16.7 GHz and ω_c^{high} = 337 GHz). The measured changes in the effective critical temperature on heating and cooling therefore depend not only on the cavity length but also on the thermal history of the sample (Supplementary Fig. 2). The observed modification of the cavity hysteresis hints at a possible scenario in which the coupling between 1T-TaS$_2$ and the cavity modes is the driving force of the effective renormalization of the transition temperature. This coupling is expected to be different in the two phases, displaying a profoundly different dielectric response.

Discussion

The cavity-dependent effect on T_c^{eff} can be rationalized within a thermodynamic picture considering how the free energies of the metallic phase (F_m) and of the dielectric phase (F_d) vary with the external temperature for different cavities (Fig. 4d). The crossing temperature between the free energies of the two phases sets the critical temperature of the metal-to-insulator transition. For simplicity, we assume F_d to be weakly dependent on temperature and cavity geometry, and subsequently consider the temperature dependence of F_m to be responsible for the phase transition. Figure 4d shows the schematic
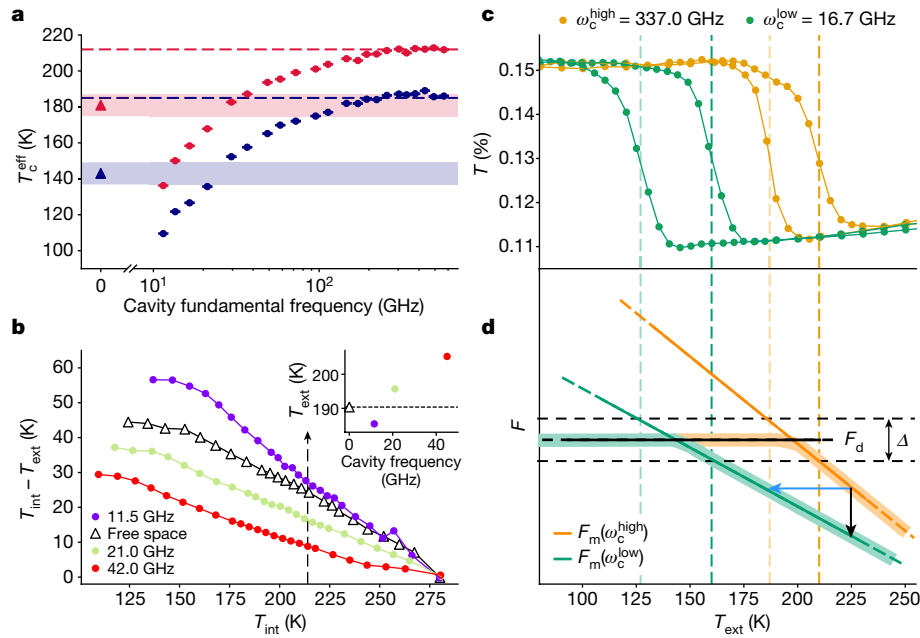
Fig. 4 | Cavity-mediated thermodynamics of the metal-to-insulator phase transition in 1T-TaS₂. a, Dependence of the effective critical temperature on the cavity fundamental frequency of the heating and cooling temperature scans. The zero-frequency point represents the effective critical temperature measured in free space; the red dashed line indicates the literature critical temperature[31] for the heating temperature scan and the blue dashed line the cooling temperature scan. The error bar associated with each temperature is the standard deviation of the effective critical temperatures estimated for three consecutive scans. **b**, Difference between the temperature measured on the sample (T_{int}) and on the cold finger (T_{ext}) as a function of the sample temperature for different values of the cavity fundamental frequency. Temperatures have been measured by heating the sample from the C-CDW phase. Inset: the effective critical temperature, defined as the cold-finger temperature at which the sample reaches the nominal critical temperature $T_{int} = 215$ K, as a function of the cavity mode. **c**, Comparison of the phase-transition hysteresis of 1T-TaS₂ within a low-frequency cavity ($\omega_c^{low} = 16.7$ GHz) and a high-frequency cavity ($\omega_c^{high} = 337$ GHz). **d**, Schematic temperature dependence of the free energy of the metallic (F_m) and the dielectric (F_d) phase at the cavity frequencies ω_c^{low} and ω_c^{high} used in **c**, The activation energy for switching the phase is indicated by Δ. The shift of the apparent transition temperature could be rationalized with a cavity-mediated renormalization of the free energy of the metallic state (black vertical arrow) or with a scaling of the sample effective temperature in analogy with the Purcell effect (blue horizontal arrow).

temperature dependence of F_m and F_d in low- and high-frequency cavities, consistent with the experimental observation in Fig. 4c.

This thermodynamical picture can be connected to the two proposed mechanisms leading to a cavity-induced modification of T_c^{eff} discussed in Fig. 1a. In the first scenario, the coupling of the cavity modes with the sample changes the energy spectrum of the collective modes in the sample. In this figure, the cavity induces a decrease in the free energy of the metallic phase with respect to the insulating phase, resulting in an effective shift of the observed transition temperature (Fig. 4d, black vertical arrow). The experimental observation would thus suggest that lowering the cavity resonance could cause a decrease in the free energy of the metallic phase and a reduction in the slope of its temperature dependence, consistent with a cavity-driven shrinking of the hysteresis.

To test whether the free-energy scenario is consistent with the experimental trends, we resort to a Dicke-based model with a single-cavity mode coupled to a continuum absorption spectrum within the GHz spectral range, in which the conductivity measurements suggest an increased dielectric response[45,46] (Methods). Importantly, under a harmonic approximation of the solid modes, the free-energy difference ΔF_m between the light–matter hybrid and the isolated systems can be understood solely in terms of the frequency-dependent polarizability of the solid, irrespective of the microscopic nature of its collective modes. The model indicates that the free energy of the metallic state F_m is lowered on lowering the cavity frequency, which is qualitatively consistent with the decrease in the effective critical temperature on reducing the cavity frequency observed experimentally (Fig. 4a). The coupling to a single-cavity mode quantitatively gives only a non-extensive contribution to the free energy[47]. The total effect on the free energy depends on the phase space of the relevant cavity modes that can be shifted within the solid spectrum. Taking into account this phase-space factor, extremely large couplings would be needed for the free-energy changes to explain the observed shifts in the transition temperature (see Methods for quantitative estimations).

In the second mechanism shown in Fig. 1a, the cavity controls the temperature of the sample and consequently the difference between the external temperature (T_{ext}) and the sample temperature (T_{int}). The reshaping of the electromagnetic density of the states driven by the cavity can induce a change in the emission spectrum of the sample and hence its temperature[48] (this scenario is represented in Fig. 4d as a renormalization of the temperature axis, blue horizontal arrow). Shorter cavities move the electromagnetic modes to higher frequencies and could effectively decouple the optically active solid modes from the external field, analogous to the Purcell effect[49]. The sample is not only in thermal contact with the cold finger through the membranes, but it is also in contact with the external photon bath at $T_{ph} = 300$ K (Fig. 1a, bottom right panel). We assume that the thermal transfer from the cold finger to the sample depends only on the difference between T_{ext} and T_{int} through a cavity-independent thermal coupling constant. Conversely, the thermal load on the sample because of the contact with the external photon bath is mediated by the cavity through a coupling constant depending on the cavity geometry (fundamental frequency ω_c and quality factor Q) and on the sample dielectric loss within the cavity range. To qualitatively illustrate the mechanism, we model the infrared spectrum of 1T-TaS₂ as a broad continuum absorption band lying in the GHz range and use the Purcell-based model to extract an effective temperature of the sample $T_{int}(\omega_c, Q)$ depending on the cavity geometry (Methods). We show that on increasing the cavity frequency—that is,

Article

by decoupling the electromagnetic active transitions in the sample from the cavity fundamental mode—the cavity induces a cooling of the sample, the effective temperature of which (T_{int}) reaches that of the cold finger (T_{ext}) at high cavity frequencies (Methods). This trend is qualitatively consistent with the effective critical-temperature trend observed experimentally with both THz (Fig. 4a) and temperature measurements (Fig. 4b).

In contrast to the first scenario, the phase-space restriction is no longer valid in this second mechanism (Fig. 1a), in which an open system is considered and thermal exchanges between material, cold finger and photon bath can happen. This, together with the experimental evidence that the cavity can coherently modify the sample temperature as a function of the frequency (Fig. 4b), suggests that the Purcell-based mechanism may be the dominant effect in the reported observation. Nevertheless, it is interesting to note that both mechanisms predict the correct dependence of the effective critical temperature on the cavity frequency. This may provide a useful guide for future quantitative theories, which should also take into account the open nature of the system as well as the nonlinear interaction between the modes in the solid.

In conclusion, we have demonstrated that the metal-to-insulator transition in 1T-TaS₂ embedded in low-energy THz cavities can be reversibly controlled by the cavity geometry. The evidence points to a scenario in which the cavity electrodynamics modifies the effective sample temperature. Our results provide a previously unknown control parameter in the phase diagram of quantum materials and enable adjusting the equilibrium collective properties in correlated materials by engineering their electromagnetic environment.

Online content

Any methods, additional references, Nature Portfolio reporting summaries, source data, extended data, supplementary information, acknowledgements, peer review information; details of author contributions and competing interests; and statements of data and code availability are available at https://doi.org/10.1038/s41586-023-06596-2.

1. Garcia-Vidal, F. J., Ciuti, C. & Ebbesen, T. W. Manipulating matter by strong coupling to vacuum fields. *Science* **373**, eabd0336 (2021).
2. Schlawin, F., Kennes, D. M. & Sentef, M. A. Cavity quantum materials. *Appl. Phys. Rev.* **9**, 011312 (2022).
3. Jarc, G. et al. Tunable cryogenic terahertz cavity for strong light–matter coupling in complex materials. *Rev. Sci. Instrum.* **93**, 033102 (2022).
4. Rini, M. et al. Control of the electronic phase of a manganite by mode-selective vibrational excitation. *Nature* **449**, 72–74 (2007).
5. Fausti, D. et al. Light-induced superconductivity in a stripe-ordered cuprate. *Science* **331**, 189–191 (2011).
6. Mitrano, M. et al. Possible light-induced superconductivity in K₃C₆₀ at high temperature. *Nature* **530**, 461–464 (2016).
7. Stojchevska, L. et al. Ultrafast switching to a stable hidden quantum state in an electronic crystal. *Science* **344**, 177–180 (2014).
8. Giusti, F. et al. Signatures of enhanced superconducting phase coherence in optimally doped Bi₂Sr₂Y₀.₀₈Ca₀.₉₂Cu₂O₈₊δ driven by midinfrared pulse excitations. *Phys. Rev. Lett.* **122**, 067002 (2019).
9. Montanaro, A. et al. Anomalous non-equilibrium response in black phosphorus to sub-gap mid-infrared excitation. *Nat. Commun.* **13**, 2667 (2022).
10. Schlawin, F., Cavalleri, A. & Jaksch, D. Cavity-mediated electron-photon superconductivity. *Phys. Rev. Lett.* **122**, 133602 (2019).
11. Curtis, J. B., Raines, Z. M., Allocca, A. A., Hafezi, M. & Galitski, V. M. Cavity quantum Eliashberg enhancement of superconductivity. *Phys. Rev. Lett.* **122**, 167002 (2019).
12. Allocca, A. A., Raines, Z. M., Curtis, J. B. & Galitski, V. M. Cavity superconductor-polaritons. *Phys. Rev. B* **99**, 020504(R) (2019).
13. Laplace, Y., Fernandez-Pena, S., Gariglio, S., Triscone, J. M. & Cavalleri, A. Proposed cavity Josephson plasmonics with complex-oxide heterostructures. *Phys. Rev. B* **93**, 075152 (2016).
14. Gao, H., Schlawin, F., Buzzi, M., Cavalleri, A. & Jaksch, D. Photoinduced electron pairing in a driven cavity. *Phys. Rev. Lett.* **125**, 053602 (2020).
15. Sentef, M. A., Ruggenthaler, M. & Rubio, A. Cavity quantum-electrodynamical polaritonically enhanced electron-phonon coupling and its influence on superconductivity. *Sci. Adv.* **4**, eaau6969 (2018).
16. Li, J. & Eckstein, M. Manipulating intertwined orders in solids with quantum light. *Phys. Rev. Lett.* **125**, 217402 (2020).
17. Latini, S., Ronca, E., De Giovannini, U., Hübener, H. & Rubio, A. Cavity control of excitons in two-dimensional materials. *Nano Lett.* **19**, 3473–3479 (2019). 2019.
18. Ashida, Y. et al. Quantum electrodynamic control of matter: cavity-enhanced ferroelectric phase transition. *Phys. Rev. X* **10**, 041027 (2020).
19. Latini, S. et al. The ferroelectric photo ground state of SrTiO₃: cavity materials engineering. *Proc. Natl Acad. Sci. USA* **118**, e2105618118 (2021).
20. Lenk, K., Li, J., Werner, P. & Eckstein, M. Dynamical mean-field study of a photon-mediated ferroelectric phase transition. *Phys. Rev. B* **106**, 245124 (2022).
21. Soykal, Ö. O. & Flatté, E. Strong field interactions between a nanomagnet and a photonic cavity. *Phys. Rev. Lett.* **104**, 077202 (2010).
22. Paravicini-Bagliani, G. L. et al. Magneto-transport controlled by Landau polariton states. *Nat. Phys.* **15**, 186–190 (2019).
23. Appugliese, F. et al. Breakdown of topological protection by cavity vacuum fields in the integer quantum Hall effect. *Science* **375**, 1030 (2022).
24. Thomas, A. et al. Large enhancement of ferromagnetism under a collective strong coupling of YBCO nanoparticles. *Nano Lett.* **21**, 4365–4370 (2021).
25. Vaidyanathan, A. G., Spencer, W. P. & Kleppner, D. Inhibited absorption of blackbody radiation. *Phys. Rev. Lett.* **47**, 1592 (1981).
26. Jones, A. S., O'Callahan, B. T., Yang, H. U. & Raschke, M. B. The thermal near-field: coherence, spectroscopy, heat transfer, and optical forces. *Prog. Surf. Sci.* **88**, 349–392 (2013).
27. Roberts, A. S., Chirumamilla, M., Thilsing-Hansen, K., Pedersen, K. & Bozhevolnyi, S. I. Near-infrared tailored thermal emission from wafer-scale continuous-film resonators. *Opt. Express* **23**, A1111–A1119 (2015).
28. Celanovic, I., Perreault, D. & Kassakian, J. Resonant-cavity enhanced thermal emission. *Phys. Rev. B* **72**, 075127 (2005).
29. Shiue, R.-J. et al. Thermal radiation control from hot graphene electrons coupled to a photonic crystal nanocavity. *Nat. Commun.* **10**, 109 (2019).
30. Vaskivskyi, I. et al. Controlling the metal-to-insulator relaxation of the metastable hidden quantum state in 1T-TaS₂. *Sci. Adv.* **1**, e1500168 (2015).
31. Wang, Y. D. et al. Band insulator to Mott insulator transition in 1T-TaS₂. *Nat. Commun.* **11**, 4215 (2020).
32. Sipos, B. et al. From Mott state to superconductivity in 1T-TaS₂. *Nat. Mater.* **7**, 960–965 (2008).
33. Nakanishi, K. & Shiba, H. Domain-like incommensurate charge-density-wave states and the first-order incommensurate–commensurate transitions in layered tantalum dichalcogenides. I. 1T-polytype. *J. Phys. Soc. Jpn* **43**, 1839–1847 (1977).
34. Nakanishi, K. & Shiba, H. Domain-like incommensurate charge-density-wave states and collective modes. *J. Phys. Soc. Jpn* **45**, 1147–1156 (1978).
35. Wilson, J. A., Di Salvo, F. J. & Mahajan, S. Charge-density waves and superlattices in the metallic layered transition metal dichalcogenides. *Adv. Phys.* **24**, 117–201 (1975).
36. Burk, B., Thomson, R. E., Clarke, J. & Zettl, A. Surface and bulk charge density wave structure in 1 T-TaS₂. *Science* **257**, 362–364 (1992).
37. Thomson, R. E., Burk, B., Zettl, A. & Clarke, J. Scanning tunneling microscopy of the charge-density-wave structure in 1T-TaS₂. *Phys. Rev. B* **49**, 16899–16916 (1994).
38. Tsen, A. W. et al. Structure and control of charge density waves in two-dimensional 1T-TaS₂. *Proc. Natl Acad. Sci. USA* **112**, 15054–15059 (2015).
39. Wang, W., Dietzel, D. & Schirmeisen, A. Lattice discontinuities of 1T-TaS₂ across first order charge density wave phase transitions. *Sci. Rep.* **9**, 7066 (2019).
40. Gasparov, L. V. et al. Phonon anomaly at the charge ordering transition in 1T-TaS₂. *Phys. Rev. B* **66**, 094301 (2002).
41. Dean, N. et al. Polaronic conductivity in the photoinduced phase of 1T-TaS₂. *Phys. Rev. Lett.* **106**, 016401 (2011).
42. McMillan, W. L. Landau theory of charge-density waves in transition-metal dichalcogenides. *Phys. Rev. B* **12**, 1187 (1975).
43. Baek, S., Sur, Y., Kim, K. H., Vojta, M. & Büchner, B. Interplay of charge density waves, disorder, and superconductivity in 2H-TaSe₂ elucidated by NMR. *New J. Phys.* **24**, 043008 (2022).
44. Svetin, D. et al. Transitions between photoinduced macroscopic quantum states in 1T-TaS₂ controlled by substrate strain. *Appl. Phys. Express* **7**, 103201 (2014).
45. Ma, Y., Hou, Y., Lu, C., Li, L. & Petrovic, C. Possible origin of nonlinear conductivity and large dielectric constant in the commensurate charge-density-wave phase of 1T-TaS₂. *Phys. Rev. B* **97**, 195117 (2018).
46. Ma, Y., Wu, D. & Wang, Z. The evidence of stacking disorder from dielectric response along the c-axis in the commensurate CDW phase in bulk 1T-TaS₂. *Solid State Commun.* **316–317**, 113946 (2020).
47. Pilar, P., De Bernardis, D. & Rabl, P. Thermodynamics of ultrastrongly coupled light–matter systems. *Quantum* **4**, 335 (2020).
48. Picardi, M. F., Nimje, K. N. & Papadakis, G. T. Dynamic modulation of thermal emission— a tutorial. *J. Appl. Phys.* **133**, 111101 (2023).
49. Purcell, E. M., Pound, R. V. & Bloembergen, N. Nuclear magnetic resonance absorption in hydrogen gas. *Phys. Rev.* **70**, 986 (1946).

Methods

Experimental details

Experimental set-up. The experimental set-up[3] is shown in Extended Data Fig. 1a. The cryogenic THz cavity shown in the inset consists of two cryo-cooled piezo-controlled semi-reflecting mirrors between which the sample is inserted. The movement of both cavity mirrors is ensured by three piezo actuators (N472–11V, Physik Instrumente) having a travel range of 7 mm and a minimum incremental motion of 50 nm with a designed resolution of 5 nm. The mirrors are mounted on copper holders, and they are cryo-cooled using copper braids directly connected to the cold finger of the cryostat. To ensure the tuning of the distance of the mirrors at cryogenic temperatures, the piezo actuators are thermally decoupled from the mirror supports. The thermal decoupling is realized by placing a PEEK disk between the piezo actuators and the mirror holders, on which the piezoelectrics act, and three ceramic cylinders. The chamber shown in Extended Data Fig. 1a (inset) is mounted on a flow cryostat with a temperature feedback circuit enabling temperature scans at fixed cavity lengths. The temperature is read both on the sample holder and on the mirror holders. The deviation in temperature is less than 1 K for a measurement at a fixed temperature.

The cavity semi-reflecting mirrors were fabricated by evaporating a thin bilayer of titanium-gold (2–15 nm) on a 2-mm crystalline quartz substrate. We measured the transmission amplitude of a single-cavity mirror to be 15% in the THz spectral range of the experiment with no apparent spectral features.

The approximately 10-μm thick 1T-TaS$_2$ sample is mounted between the two mirrors in a copper sample holder directly connected to the cold finger of the cryostat and sealed between two silicon nitride membranes (grown by low-pressure chemical vapour deposition) with a window size of 11×11 mm^2 and a thickness of 2 μm. The membranes are supported on a 13×13 mm^2 silicon frame and do not show any spectral dependence in the THz spectral range used.

We used broadband THz spectroscopy to characterize the metal-to-insulator transition for different cavity settings. Single-cycle THz pulses are generated by the acceleration of the photoinduced carriers in a large-area GaAs-based photoconductive antenna. The photoexcitation is achieved by pumping the photoconductive antenna with an ultrashort laser pulse (50 fs pulse duration, 745 nm central wavelength, 6 μJ per pulse energy) from a commercial 50-kHz pulsed laser + optical parametric amplifier system (Pharos + Orpheus-F, Light Conversion). The collimated THz beam emitted is then focused on the sample mounted inside the cavity (Extended Data Fig. 1a, inset). We estimated the THz spot diameter at the focus position to be about 1.5 mm, which is smaller than the lateral dimensions of the 1T-TaS$_2$ crystal (4 mm × 4 mm). The field transmitted through the sample is probed by standard electro-optical sampling in a 0.5-mm ZnTe crystal with a weak read-out pulse (50 fs pulse duration, 745 nm central wavelength, <100 nJ per pulse energy). We present in Extended Data Fig. 1b the measured electric field of the generated THz pulse and its calculated Fourier spectrum in Extended Data Fig. 1c. The input field is a nearly single-cycle THz pulse with a spectral content up to 6 THz, as highlighted in the logarithmic scale plot in Extended Data Fig. 1c (inset). We estimated the signal-to-noise of the detected THz field to be 4.6×10^4 and a temporal phase stability of less than or equal to 30 fs.

Sample preparation. The single crystals from which flakes are exfoliated are grown from the elements (purity of Ta = 99.95% and S = 99.999%) by the vapour-phase transport method at 850 °C with 1.5 mg cm^{-3} excess S, quenched from the growth temperature to a room temperature water bath to retain the 1T polytype.

Single-crystal X-ray diffraction analysis confirms that the pure single 1T phase is retained after the quench ($a = b = 3.357$, $c = 5.91$), with the Ta:S composition ratio determined by energy-dispersive X-ray spectroscopy to be 33:66 ± 1 atomic %. Scanning tunnelling microscopy measurements show rare-earth impurities on the surface-layer content consistent with the impurity concentrations given by the supplier (Alfa Aesar, Merck).

Measurement protocols and data analysis

Characterization of the empty cavity. To estimate the quality factor of the cavity, we characterized the response of the empty cavity—that is, when the THz field passes through only the silicon nitride membranes within the mirrors. The quality factor quantifies the photon lifetime inside the cavity and, subsequently, the coupling strength between the cavity mode and the targeted material excitation, which is ruled by the bare cavity dissipations.

The two cavity mirrors were set parallel to each other and perpendicular to the THz beam by aligning the multiple reflections of the pump optical beam, which propagates collinearly with the THz beam.

In Extended Data Fig. 2, we show the time-domain THz field transmitted through the Fabry–Pérot cavity (Extended Data Fig. 2a) and the corresponding spectral content (Extended Data Fig. 2b) for three representative values of the cavity fundamental mode ω_c among the one used in the experiment (ω_c = 53, 77 and 106 GHz). The cavity transmission spectra plotted in Extended Data Fig. 2b were obtained by taking the ratio of the Fourier spectrum of the time-domain traces (Extended Data Fig. 2a) and the reference free-space spectrum (Extended Data Fig. 1d). The cavity transmission spectra exhibit the interference Fabry–Pérot modes with a tunable fundamental frequency set by the cavity length.

For the three representative cavities shown in Extended Data Fig. 2, we estimated the quality factors Q to be 3.3, 3.6 and 3.5 for the 53-, 77-, and 106-GHz cavities, respectively. The quality factors were calculated as the ratio of the fundamental cavity frequency and its bandwidth defined as the full width at half maximum of the transmission peak of the fundamental mode.

This estimation shows that, for all the cavity lengths that we studied, the bare quality factor (and hence the incoherent photon losses) can be considered independent of the cavity frequency.

Characterization of the sample thermalization time. To show that all the measurements have been performed in a stationary regime, we estimated the thermalization time of the sample by delaying the THz acquisition by different amounts of time. As shown in Extended Data Fig. 3, no substantial variation in the effective critical temperature and the slope of the phase transition occurs for $\Delta t \geq 2$ min. This is because all the measured THz traces in the experiment are the result of a 20-min integration time at each temperature step with a 5-min waiting time before the first THz acquisition. Therefore, we can safely rule out that the observed inhomogeneous-like feature of the phase transition is because of a measurement waiting time less than the sample thermalization, and it can be probably ascribed to intrinsic inhomogeneities of the sample, which can smear out the phase transition[43]. Another factor that could be responsible for the smearing out of the metal-to-insulator transition in single-crystal 1T-TaS$_2$ samples is substrate strain. Strain plays an important part in the metal-to-insulator transition and can shift and broaden the transition temperature substantially[44]. Furthermore, when mounted on membranes, the homogeneity of the temperature, in particular the in-plane one, may also broaden the transition.

Determination of the effective critical temperature. Here we present the method used to extract the effective critical temperatures from the THz transmission data.

Extended Data Fig. 4a shows the temperature evolution of the integrated low-frequency transmission (0.2 THz < ω < 1.5 THz) associated with the onset of the metallicity. Extended Data Fig. 4b shows the temperature evolution of the transmitted spectral weight around the 1.58-THz phonon integrated into the range of 1.53–1.62 THz. This integration range corresponds to the phonon bandwidth.

Article

To estimate the effective critical temperature at each cavity length, we interpolated the metallic and phononic temperature responses and calculated the derivative of the interpolated curve. The temperature derivative obtained for the free-space sample is shown in Extended Data Fig. 4a,b (bottom panels) for the metallic and phononic responses, respectively.

We set the effective critical temperature of the phase transition (T_c^{eff}) to be the maximum of the derivative of the interpolated curve. The error associated with each T_c^{eff} is the standard deviation of the effective critical temperatures estimated for three consecutive scans. The robustness of this procedure is validated by the fact that the effective critical temperatures estimated from the metallic response are compatible with those estimated from the phonon spectral response.

Theoretical models

Free-energy picture. We introduce here the phenomenological model providing a qualitative estimation of the renormalization of the free energy of the metallic NC state due to cavity electrodynamics.

Let us consider a solid with given dielectric properties, characterized by the polarizability $\alpha(\omega)$, which determines the response of the transverse polarization density to the electric field, $\mathbf{P}(\omega) = \varepsilon_0 \alpha(\omega)\mathbf{E}(\omega)$. The polarizability $\alpha(\omega)$ is related to the relative dielectric function $\varepsilon(\omega)$ as $\varepsilon(\omega) = 1 + \alpha(\omega)$. A non-zero polarizability implies that there are modes in the solid that can hybridize with the electromagnetic field, which in turn leads to a change in the free energy when the system is put in the cavity. To understand the effect of the cavity on the free energy of the system, we evaluate the difference

$$\Delta F = F_{tot} - F_{mat} - F_{cav} \tag{1}$$

between the total free energy of the coupled system (F_{tot}) and the free energies of the uncoupled solid (F_{mat}) and of the electromagnetic field (F_{cav}). A key observation is that as long as the solid is approximately described by a harmonic theory, ΔF can be determined from the knowledge of the experimentally accessible dielectric function alone, independent of microscopic details such as the precise nature of the electromagnetically active modes. In short, in a harmonic theory, we can exactly integrate the modes of the solid, so that the resulting effective action of the cavity, which then determines ΔF, is given in terms of the linear response functions of matter.

We will make a further simplification in line with the present experimental setting and assume that the volume V_m of the solid is small compared with the cavity volume V, that is, $V_m/V \ll 1$. This approximation is valid for the experimental setting because the cavities used have fundamental frequencies in the low THz region, and the sample thickness is about 10 μm. With this approximation, as shown below, for a single-cavity mode with fundamental frequency ω_c, the free-energy renormalization ΔF due to the light–matter coupling (equation (1)) is given by $\Delta F(\omega_c, T) = \frac{V_m}{V} f(\omega_c, T)$, where

$$f(\omega_c, T) = \frac{1}{\pi} \int_0^\infty d\omega \, \alpha''(\omega)\omega \frac{b(\omega_c, T)\omega_c - b(\omega, T)\omega}{\omega_c^2 - \omega^2}. \tag{2}$$

In equation (2), $b(\omega, T) = (e^{\omega/T} - 1)^{-1}$ is the Bose function and $\alpha''(\omega)$ is the imaginary part of the solid polarizability (dielectric loss).

The change in total free energy ΔF is a thermodynamically extensive quantity, which arises from the coupling to a continuum of cavity modes with transverse momentum q and a discrete mode index n (Extended Data Fig. 5a). For simplicity, instead of summing equation (2) over all cavity modes $\omega_c \equiv \omega_{q,n}$, we will first analyse the single-mode result (equation (2)) for the lowest cavity frequency ($\omega_c = \pi c/L$, where L is the cavity length) to understand the qualitative functional dependence of ΔF on the temperature and the cavity parameters. To estimate the order of magnitude of the total effect of all modes, we will multiply the result

with a phase-space factor that counts the number of modes N_{modes} that are affected by the cavity.

To analyse the free-energy renormalization (equation (2)), we assume that the solid polarizability $\alpha(\omega)$ gives rise to a broad continuum absorption band that can be fitted by the response of a strongly damped oscillator:

$$\alpha(\omega) = \alpha(0) \frac{\Omega^2}{\Omega^2 - \omega^2 - i\omega\gamma}, \tag{3}$$

where Ω corresponds to the central frequency of the mode of the material, γ is the linewidth and $\alpha(0)$ is the contribution of the mode to the static polarizability. The latter also measures the total spectral weight in the absorption band and therefore serves as a phenomenological measure of the effective coupling strength. The dielectric loss $\alpha''(\omega)$ adopted for the estimations is shown in Extended Data Fig. 5b. We set a central frequency $\Omega = 15$ GHz and a frequency damping $\gamma = 20$ GHz so that no significant contribution to the solid dielectric loss is present in the THz region ($\omega > 0.1$ THz).

We show in Extended Data Fig. 5c the dependence of the free-energy renormalization of the metallic phase (equation (2)) as a function of the cavity frequency ω_c when the latter is swept through the mode centred at Ω. The model indicates that the free energy of the metallic state is lowered on lowering the cavity frequency, which is qualitatively consistent with the decrease in the effective critical temperature on reducing the cavity frequency observed experimentally. The renormalization of the metallic free energy is larger for larger temperatures, indicating that it is related to the thermal population of the low-energy mode. We stress that the temperature in the experiment is well above Ω. Extended Data Fig. 5d shows the free-energy renormalization as a function of temperature for different cavity frequencies ω_c below and above the resonance $\omega_c = \Omega$. The free energy of the metallic phase is lowered and becomes steeper when the cavity frequency is lowered (that is, opening the cavity). This trend is consistent with the interpretation of the experimental observation in the main text highlighted in Fig. 4d.

However, the absolute changes in the total free energy are expected to be rather small. As mentioned above, the single-mode result $\Delta F(\omega_c, T) = \frac{V_m}{V} f(\omega_c, T)$ should be integrated over all modes or, for a simple estimate, multiplied with a phase-space factor N_{modes}. If the latter is simply taken to account for all modes below a certain cutoff ω_{cut} in a volume V, we have $N_{modes} = V/\lambda_{cut}^3$, up to constants of order 1. Therefore, the free-energy change $N_{modes} \times \frac{V_m}{V} f(\omega_c, T)$ per volume V_m is given by the amount $f(\omega_c, T)$ per volume λ_{cut}^3. The changes of $f(\omega_c, T)$ on modifying the cavity frequency are of the order of $\alpha(0)\Omega$ (Extended Data Fig. 5c,d), thus corresponding to an energy density $\alpha(0)\Omega/\lambda_{cut}^3$. This value has to be compared with the condensation energy density of the phase transition, which is $Q \approx 6$ J mm$^{-3} \approx 3.6 \times 10^{10}$ eV μm^{-3} (ref. 50). With Ω in the submillielectronvolt range, very large couplings $\alpha(0)$ would be needed, even with a cutoff λ_{cut} in the optical range (which is an upper bound, as optical frequencies are hardly affected by the present cavity setting).

We, therefore, conclude that although the free-energy renormalization in the cavity ΔF follows the correct trend (lowering the free energy of the nearly commensurate phase as the cavity is opened), it is not sufficient to explain the experimental observation. Although it will be interesting to investigate future theoretical interpretations that go beyond the harmonic theory, this puts more emphasis on the second mechanism (Purcell-like effect) discussed in this study.

Finally, let us conclude with the derivation of equation (2). Let us start with a general harmonic model in which one mode of the electromagnetic field couples to a continuum of modes in the solid. The Hamiltonian is a general Dicke-type Hamiltonian:

$$H = \frac{1}{2} \sum_a \left(\Omega_a^2 \left[p_a + \frac{\kappa\gamma_a}{\Omega_a^2}\Pi \right]^2 + x_a^2 \right) + \frac{1}{2}(\Pi^2\omega_q^2 + X^2), \tag{4}$$

where X and Π are the canonical quadratures of the electromagnetic field, and p_a and x_a are the quadratures of the modes in the solid. The solid normal modes have frequencies Ω_a in the absence of the coupling to the cavity field. The electromagnetic field quadrature Π is related to the vector potential (which is spatially homogeneous throughout the solid) according to the relation

$$\hat{A} = \hat{n}\sqrt{\frac{1}{\varepsilon_0 V}}\,\Pi, \tag{5}$$

where V indicates the cavity mode volume and $\hat{n}$ the polarization direction. The electric field is connected to the vector potential by the temporal derivative $E = -\dot{A}$. The complete square light–matter coupling in equation (4), with coupling constants γ_a, corresponds to a minimal coupling of the modes in the solid to the vector potential. The coupling between the solid oscillators and the single-cavity mode scales as $\kappa\gamma_a$ where $\kappa^2 = V_m/V$ is the volume fraction of the cavity filled with the solid. Note that, as mentioned above, the final result for ΔF will be expressed in terms of the polarizability, so that the detailed choice of the parameters Ω_a and γ_a does not enter.

The aim is now to calculate the free-energy difference ΔF within this model. Denoting by η_α and $\eta_\alpha^{(0)}$ the normal modes energies of the coupled and uncoupled systems, respectively, the free-energy difference (equation (1)) is simply given by

$$\Delta F = \frac{1}{\beta}\sum_\alpha [\ln(1 - e^{-\beta\eta_\alpha}) - \ln(1 - e^{-\beta\eta_\alpha^{(0)}})], \tag{6}$$

where $\ln(1 - e^{-\beta\eta})/\beta$ is the free energy of an oscillator with frequency η. The η_α^2 are given by the eigenvalues of the dynamical matrix $\mathcal{D}$ corresponding to the Hamiltonian (equation (4))

$$\mathcal{D} = \begin{pmatrix} \tilde{\omega}_c^2 & \kappa\gamma_1 & \kappa\gamma_2 & \cdots \\ \kappa\gamma_1^* & \Omega_1^2 & 0 & \\ \kappa\gamma_2^* & 0 & \Omega_2^2 & \\ \vdots & & & \ddots \end{pmatrix}. \tag{7}$$

Here $\tilde{\omega}_c^2$ is the shifted cavity frequency $\tilde{\omega}_c^2 = \omega_c^2 + \kappa^2\sum_a \frac{|\gamma_a^2|}{\Omega_a^2}$ as a consequence of the coupling with the solid degrees of freedom. We determine these normal modes perturbatively in the solid volume fraction $\kappa^2 \ll 1$. The perturbative expansion for the cavity mode (entry 0 in equation (7)) reads

$$\eta_0^2 = \omega_c^2 + \kappa^2\sum_a \frac{|\gamma_a^2|}{\Omega_a^2} + \kappa^2\sum_a \frac{|\gamma_a^2|}{\omega_c^2 - \Omega_a^2}, \tag{8}$$

whereas for the matter modes, we have

$$\eta_a^2 = \Omega_a^2 + \kappa^2\frac{|\gamma_a^2|}{\Omega_a^2 - \omega_c^2}. \tag{9}$$

We can then linearize equation (6) in $\delta\eta$, leading to $\Delta F = \kappa^2\sum_a b(\eta_\alpha^{(0)})\delta\eta_\alpha$, and insert the perturbative expressions of the cavity (equation (8)) and solid (equation (9)) eigenmodes. With some straightforward manipulations, this gives the result of equation (2), with the function $\alpha''(\omega)$ of the form

$$\alpha''(\omega) = \pi\sum_a \frac{|\gamma_a|^2}{2\,\Omega_a^3}[\delta(\omega - \Omega_a) - \delta(\omega + \Omega_a)]. \tag{10}$$

Finally, we need to confirm that equation (10) is precisely the imaginary part of the polarizability within the model of equation (4). A simple link is made using the dielectric loss. When the system is

driven with a time-dependent field, the absorbed energy per volume is the time average of $\mathbf{E}(t)\partial_t\mathbf{P}(t)$. With the above definition of the polarizability, the loss under a field $A(t) = \hat{n}\,(A_\omega e^{-i\omega t} + A_\omega^* e^{i\omega t})$ is

$$\Gamma(\omega) = 2\omega^3\varepsilon_0\alpha''(\omega)|A_\omega|^2. \tag{11}$$

By contrast, in equation (4), we can calculate the energy absorption due to a time-dependent classical vector potential, which using equation (5) is introduced by replacing $\Pi \to \Pi + \sqrt{V\varepsilon_0}A(t)$. Fermi's golden rule (or equivalently the Kubo linear response formalism) gives

$$\begin{aligned} \Gamma_A(\omega) &= |A_\omega|^2 2\omega\sum_a |\gamma_a|^2\chi_{aa}''(\omega)\varepsilon_0 V\kappa^2 \\ &= V_m |A_\omega|^2 2\omega\sum_a |\gamma_a|^2\chi_{aa}''(\omega)\varepsilon_0, \end{aligned} \tag{12}$$

with the spectral function

$$\chi_{aa}''(\omega) = \frac{\pi}{2\Omega_a}[\delta(\omega - \Omega_a) - \delta(\omega + \Omega_a)] \tag{13}$$

of the single mode a. Comparing equations (11) and (12) shows that equation (10) is the result of the polarizability.

Control of dissipations through cavity electrodynamics. Here we discuss the Purcell-like scenario, that is, the mechanism in which the observed changes in the effective critical temperature could be related to a cavity control of the dissipations, analogous to the Purcell effect. In this scenario, the reshaping of the electromagnetic density of states at the sample position because of the cavity electrodynamics could result in a modification of the thermal load of the sample and subsequently of its temperature.

To estimate this effect, we proceed as indicated in Extended Data Fig. 6a. The sample is not only in thermal contact with the cold finger through the membranes, but it is also in thermal contact with the external photon bath at $T_{ph} = 300$ K. We assume that the thermal transfer from the cold finger to the sample depends only on the difference between the cold-finger temperature (T_{ext}) and the sample effective temperature (T_{int}). Conversely, we assume that the thermal load on the sample because of the contact with the external photon bath is mediated by the cavity, similar to the Purcell effect. With these hypotheses, we can write two rate equations describing, respectively, the cavity-independent heat flow between the cold finger and the sample:

$$Q_{ext-int} = K_{ext-int}(T_{ext} - T_{int}), \tag{14}$$

and the cavity-mediated heat transfer between the sample and the external photon bath:

$$Q_{ph-int}(\omega_c, Q) = K_{ph-int}(\omega_c, Q)(T_{ph} - T_{int}). \tag{15}$$

In the previous equations, $K_{ext-int}$ represents the cavity-independent coupling constant between the cold finger and the sample, whereas $K_{ph-int}(\omega_c, Q)$ is the coupling constant between the sample and the photon bath, which depends on the cavity geometry—that is, on the fundamental frequency ω_c and on the quality factor Q.

The coupling constant $K_{ph-int}(\omega_c, Q)$ between the sample and the photon bath can be expressed as the joint density of states of the solid $\rho_{Solid}(\omega)$ and of the cavity $\rho_{Cavity}(\omega_c, Q)(\omega)$, with the latter multiplied by the Boltzmann distribution (k_B) at the photon-bath temperature $T_{ph} = 300$ K:

$$K_{ph-int}(\omega_c, Q) = \int_0^\infty d\omega\, \rho_{Cavity}(\omega_c, Q)(\omega)\rho_{Solid}(\omega)e^{-\frac{\omega}{k_B T_{ph}}}. \tag{16}$$

Considering a continuum broad mode centred at $\Omega = 15$ GHz and with a spectral linewidth $\gamma = 20$ GHz (as for the free-energy model described in the previous section), the solid density of states associated with the excitations of the material can be expressed through the dielectric loss per unit frequency as

$$\rho_{\text{Solid}}(\omega) = \frac{\alpha''(\omega)}{\Omega} = \alpha(0)\frac{\Omega\gamma\omega}{(\omega^2 - \Omega^2)^2 + (\gamma\omega)^2}. \tag{17}$$

Conversely, the multimode cavity density of states takes the form

$$\rho_{\text{Cavity}}(\omega_c, Q)(\omega) = \sum_{n=0}^{+\infty} \frac{\gamma_{\text{cav}}}{(\omega - n\omega_c)^2 + (\gamma_{\text{cav}})^2}, \tag{18}$$

where γ_{cav} represents the linewidth of the bare cavity, which is related to the quality factor Q by the relation $Q = \omega_c/\gamma_{\text{cav}}$. The quality factor of the empty cavity is set by the experimental conditions (see section 'Characterization of the empty cavity').

In Extended Data Fig. 6b, we present a plot of the solid density of state and of the cavity density of states multiplied by the Boltzmann distribution at the photon-bath temperature $T_{\text{ph}} = 300$ K.

Under stationary conditions, the thermal flow from the cold finger to the sample $Q_{\text{ext-int}}$ equals the cavity-mediated heat transfer between the sample and the photon bath $Q_{\text{ph-int}}(\omega_c, Q)$, that is, $Q_{\text{ext-int}} + Q_{\text{ph-int}}(\omega_c, Q) = 0$. At equilibrium, we can subsequently calculate an effective sample temperature $T_{\text{int}}(\omega_c, Q)$, which takes the form

$$T_{\text{int}}(\omega_c, Q) = \frac{K_{\text{ph-int}}(\omega_c, Q)T_{\text{ph}} + K_{\text{ext-int}}T_{\text{ext}}}{K_{\text{ph-int}}(\omega_c, Q) + K_{\text{ext-int}}}. \tag{19}$$

The temperature ratio between the sample and the cold finger $T_{\text{int}}(\omega_c, Q)/T_{\text{ext}}$ as a function of the cavity fundamental frequency is plotted in Extended Data Fig. 6c for different cold-finger temperatures. We stress that the renormalization of the sample effective temperature scales with the cavity–solid joint density of states $K_{\text{ph-int}}(\omega_c, Q)$, and hence with the total spectral weight within the solid absorption band $\alpha(0)$. A larger renormalization of the temperature of the sample is therefore expected for a larger oscillator strength of the modes of the solid.

Although the density of states of the electromagnetic field can be enhanced inside the optical cavity with respect to free space, potentially enhancing radiative transitions in materials in resonance with the cavity, shorter cavities move the electromagnetic modes to higher frequencies and could effectively decouple the optically active modes of the material from the external field, similar to the Purcell effect.

We note that, on increasing the cavity frequency–that is, by reducing the coupling of the electromagnetic active modes from the cavity fundamental mode, the model predicts a decrease in the temperature ratio $T_{\text{int}}(\omega_c, Q)/T_{\text{ext}}$, consistent with a decrease in the effective temperature of the sample (Fig. 4b). This trend is qualitatively consistent with that observed experimentally with THz spectroscopy (Fig. 4a)–that is, an increase in the effective critical temperature (T_c^{eff}) on increasing the cavity frequency.

Moreover, on lowering the cavity frequency, the coupling between the active optical transitions in the material and light can be enhanced within a frequency range, and the cavity may effectively enhance the absorption of the external blackbody radiation from the sample[51], heating the sample with respect to free-space conditions. Our measurements indicate that the cavity frequency range explored in the experiments is higher compared with that of the relevant absorption modes in the solid.

As highlighted in Extended Data Fig. 6c, the cavity-mediated modification of the sample photon-bath dissipations is more efficient at lower cold-finger temperatures–that is, when the difference between the temperature of the photon thermal bath (T_{ph}) and T_{ext} is larger. As the phase transition on cooling 1T-TaS$_2$ occurs at a lower temperature with

respect to the phase transition on heating it, we expect the Purcell-like effect to be more efficient in shifting the apparent cooling critical temperature with respect to that of heating. This prediction could justify the effective shrinking of the hysteresis observed by sweeping the cavity mode from lower to higher frequencies (Fig. 4c).

In Extended Data Fig. 6d, we show that the trend presented in Extended Data Fig. 6c is qualitatively independent of the thermal coupling constant between the sample and the cold finger $K_{\text{ext-int}}$. A change in $K_{\text{ext-int}}$ in the cavity frequency range used acts only as a scaling factor of the cavity frequency trend. The results shown in Extended Data Fig. 6d have been calculated for a representative cold-finger temperature $T_{\text{ext}} = 80$ K.

Last, we point out that the renormalization of the sample effective temperature induced by the cavity is more efficient when the thermal coupling between the sample and the cold finger is smaller. At very high thermal couplings $K_{\text{ext-int}}$, we expect the contribution to the temperature of the sample of the cavity-dependent interaction with the photon bath, and hence the renormalization of T_{int}, to be negligible.

Further studies are needed to provide a quantitative estimate of the cavity-dependent total radiative heat load experienced by the sample in the optical cavity. An increased sensitivity in this respect could be provided by cavity design featuring a better thermal isolation between the sample and the cold finger.

Temperature measurements within the cavity

The temperature indicated in all the reported measurements is the cold-finger read-out. When performing THZ optical measurements, this choice is mandatory because any thermosensitive device introduced in the cavity would not only impede the THz transmission but also modify the sample environment. By contrast, measuring the actual temperature of the sample is crucial to discriminate between the two cavity-mediated scenarios that we proposed (see section 'Theoretical models').

To this aim, we directly measured the temperature–of both the membrane and the sample–in the cavity by sealing a custom-made 20 μm Cr–Al junction within the membranes. In Extended Data Fig. 7, we show a picture of the thermocouple arrangement within the sample mount. Importantly, to not have offsets in the temperature read-out, all the wires connecting the junction to the output of the head of the cryostat were made of Cr and Al of around 120 μm. The only discontinuity point is represented by the gold male–female connectors at the output of the sample holder, which, as we verified, give no temperature discrepancy.

We highlight that, in this experimental setting, the THz optical measurements cannot be performed; it is therefore not possible to monitor the THz response of the sample as a function of its actual (measured) temperature. All the temperature measurements discussed below must be then considered a separate characterization of the temperature of the sample in a cavity geometry that is nevertheless identical to that which is used in all the THz measurements discussed in the paper.

Finite-elements simulations of incoherent heating

To estimate the effect of the incoherent thermal radiation within the cavity, we performed finite-elements simulations using the COMSOL MULTIPHYSICS software. By simulating the incoherent thermal load at the membrane position, we obtained the thermal profile of the membrane for different cavity configurations.

Let us model the membrane as a grey body having emissivity ε, reflectivity ρ, absorptivity α and temperature T, and let us assume the incoherent radiative properties of the membrane to be fully described by these four parameters ε, ρ, α and T. The net inward heat flux Q at a certain point x on the surface of the membrane is given by the difference between the total arriving radiative flux G (irradiation) and the total outgoing radiative flux J (radiosity):

$$Q(x) = G(x) - J(x). \tag{20}$$

The radiosity J is the sum of the reflected and emitted radiation from the membrane and can be described through the Stefan–Boltzmann equation as

$$J(x) = \rho G(x) + \varepsilon \sigma T^4. \tag{21}$$

By imposing that the membrane is in thermodynamical equilibrium with the surroundings—that is, the emissivity ε is equal to the absorptivity α—we can rewrite the reflectivity ρ as

$$\alpha = \varepsilon = 1 - \rho. \tag{22}$$

Thus, the net inward radiative flux of the membrane can be expressed only as a function of G, ε and T as

$$Q(x) = \varepsilon (G(x) - \sigma T^4). \tag{23}$$

Equation (23) has been used in COMSOL as a radiation boundary condition for the surface of the membrane.

The total surface radiation G includes radiation from both the ambient surroundings and other surfaces. A generalized equation for the irradiative flux is

$$G(x) = G_m(x) + F_{amb}(x)\sigma T_{amb}^4, \tag{24}$$

where G_m is the mutual irradiation arriving from other surfaces in the modelled geometry, $T_{amb} = 300$ K is the temperature of the surrounding environment schematized as a radiative black body and F_{amb} is the ambient view factor. The latter parameter describes the portion of the view from each point that is covered by ambient conditions. Conversely, G_m is determined by the geometry and the local temperatures of the surrounding surface boundaries. Including the expression of the irradiation G in equation (23), the general expression of the net radiative load at the specific point x on the membrane is

$$Q(x) = \varepsilon (G_m(x) + F_{amb}(x)\sigma T_{amb}^4 - \sigma T^4). \tag{25}$$

This equation has been used by COMSOL to compute the net radiative transfer at each point x on the surface of the membrane. Equation (25) results in a linear equation system in $Q(x)$ that must be solved in parallel with the heat transfer equation for the temperature T:

$$Q(x) = -k\nabla^2 T(x) \tag{26}$$

to extract the thermal profile of the membrane $T(x)$. In equation (26), k represents the thermal conductivity of the membrane.

First, we discuss the simulated thermal profile of a single silicon nitride membrane held in free space. For simplicity, we assumed a two-dimensional circular geometry for the membrane. We imposed the boundary conditions to have the edge of the membrane at the same temperature as that of the cold finger. The thermal profile along the radial coordinate of the free-space membrane will therefore be controlled by the balance between the emissivity ε of the membrane and the thermal load due to ambient black body radiation at $T_{amb} = 300$ K. For the simulations, we set the silicon nitride emissivity at $\varepsilon = 0.3$ (ref. 52) supposing no wavelength dependence across the mid-infrared, in which the blackbody radiation of the membrane within the temperature range

(80–300 K) is located. Extended Data Fig. 8 shows the simulated thermal profile of the membrane in free space, together with a cut along the radial direction.

We highlight that by setting the cold-finger temperature at the temperature at which the phase transition in 1T-TaS$_2$ is observed in free space ($T_{ext} = 180$ K), we can retrieve a temperature in the middle of the membrane (and hence at the sample position) corresponding to T_c reported in the the literature. The simulation, therefore, confirms the assumption that the measured rigid shift of the free-space critical temperature (Fig. 1b,c) with respect to that reported in the literature has to be attributed to the high thermal impedance of the silicon nitride membranes between which the sample is embedded, which does not enable them to efficiently re-radiate the ambient blackbody radiation.

As shown in Extended Data Fig. 9, the simulations confirm that the incoherent thermal load on the membranes is not significantly influenced by the distance between the cryogenic mirror mounts. This further excludes a trivial scenario in which the geometrical variation of the cavity mounts screens the ambient radiation and subsequently changes the temperature of the membrane.

Data availability
Raw hysteretic curves as a function of the cavity frequency (Fig. 4a) as well as the raw single THz scans of Figs. 3b and 4c are provided in the Supplementary Information. Further datasets collected for this study are available from the corresponding author upon reasonable request.

50. Guy, D. R. P., Ghorayeb, A. M., Bayliss, S. C. & Friend, R. H. in *Charge Density Waves in Solids* Lecture Notes in Physics Vol. 217 (eds Hutiray, G. & Sólyom, J.) 80–83 (Springer, 1985).
51. Goy, P., Raimond, J. M., Gross, M. & Haroche, S. Observation of cavity-enhanced single-atom spontaneous emission. *Phys. Rev. Lett.* **50**, 1903–1906 (1983).
52. Russell, R. W., Chatelain, M. A., Hecht, J. H. & Stephens, J. R. Si$_3$N$_4$ emissivity and the unidentified infrared bands. In *IAU Symposium, Interstellar Dust: Contributed Papers* Vol. 135 (eds Allamandola, L. J. & Tielens, A. G. G. M.) 157–162 (1989).

Author contributions G.J., S.Y.M. and A.M. performed the experiments with support from F.G. and E.M.R. G.J. analysed the data with support from S.Y.M. M.E., D.F. and F.F. conceived and developed the theoretical models with support of D.M. and P.P. G.J. performed the finite-element simulations of incoherent thermal heating. R.S. developed the micrometric thermocouple junction for the temperature measurements within the cavity. S.D.Z. fabricated the silicon nitride membranes and the semi-reflecting cavity mirrors. D.M. provided the 1T-TaS$_2$ samples. S.W. provided the THz emitters and guided the THz set-up. G.J., D.F., A.M., M.E. and F.F. wrote the paper with contributions from all the other authors. D.F. conceived and managed the project.
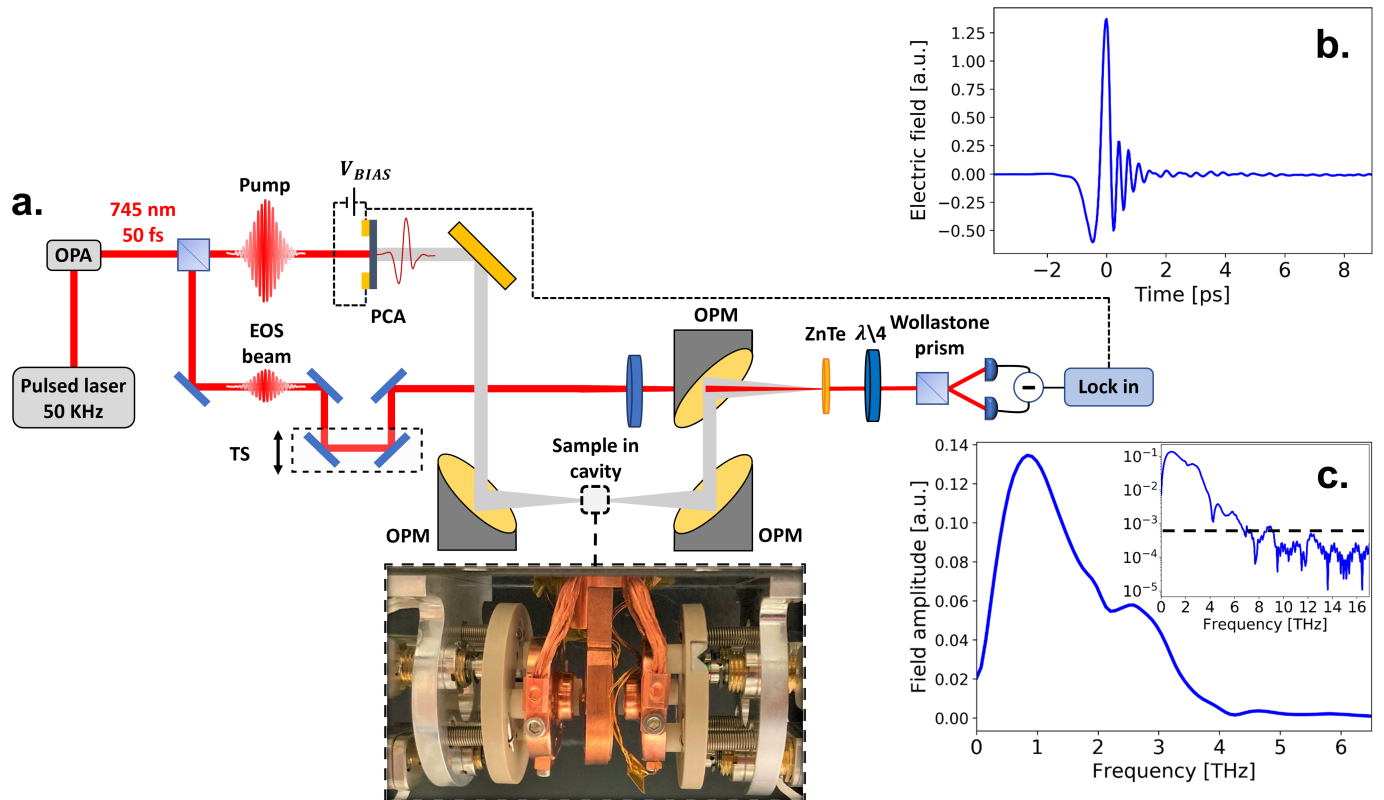
Extended Data Fig. 1 | Experimental set-up. a. Sketch of the THz time domain spectrometer. In the inset, the photograph of the tunable cryogenic cavity composed of two cryo-cooled moving mirrors within which the sample is embedded. **b.** Free-space nearly single-cycle THz field employed in the experiments detected trough Electro-Optical Sampling (EOS) in a 0.5 mm ZnTe crystal. **c.** Fourier transform of the nearly single-cycle THz field in free space. In the inset, the Fourier spectrum is plotted in logarithmic scale to highlight the spectral content of the THz field up to ∼ 6 THz. The black dashed line in the logarithmic plot indicates the noise level.
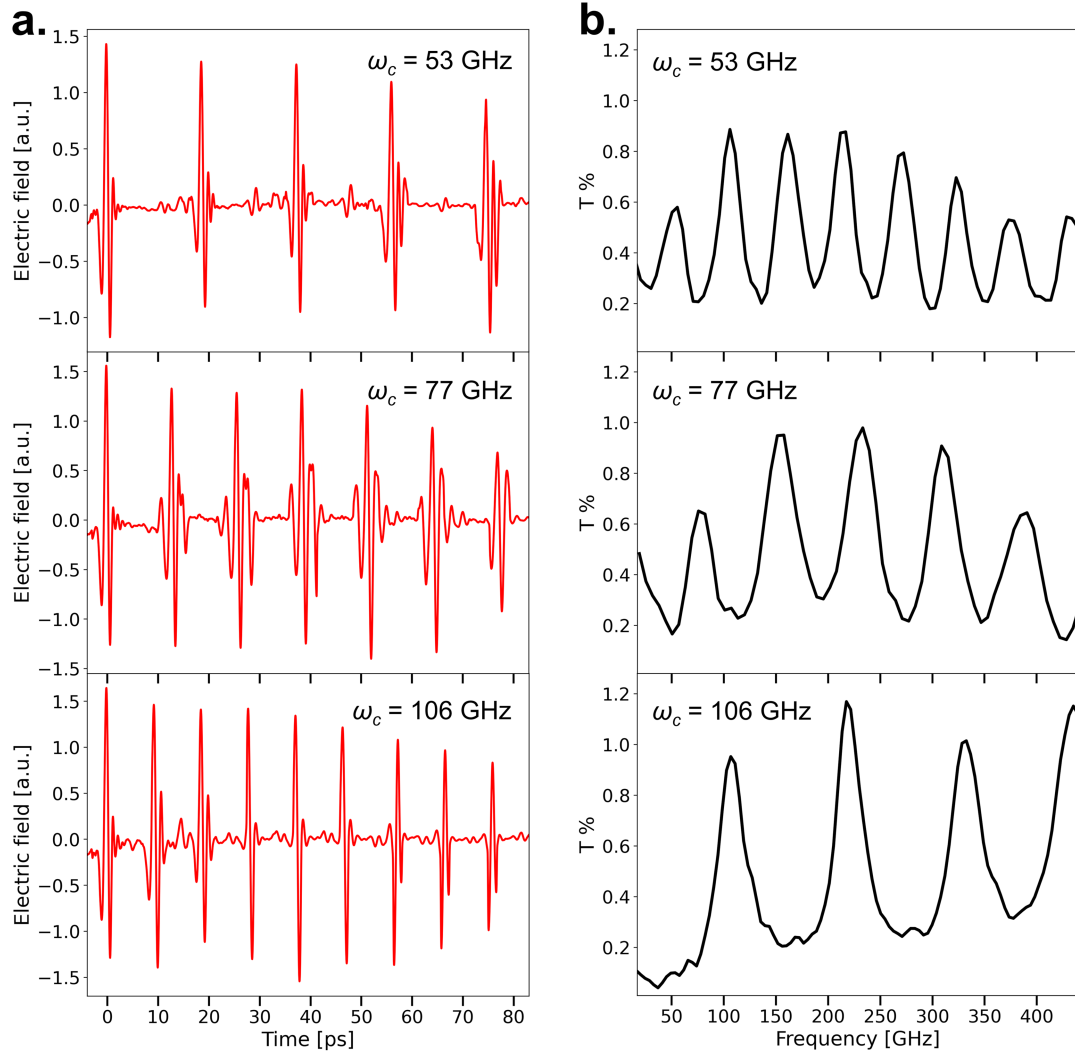
Extended Data Fig. 2 | THz characterization of the empty cavity. a. Time domain THz fields measured at the output of the empty cavity for three representative cavity frequencies ω_c indicated in legend. **b**. Cavity transmission spectra calculated from the fields shown in a. proving the tunability of the cavity fundamental mode.
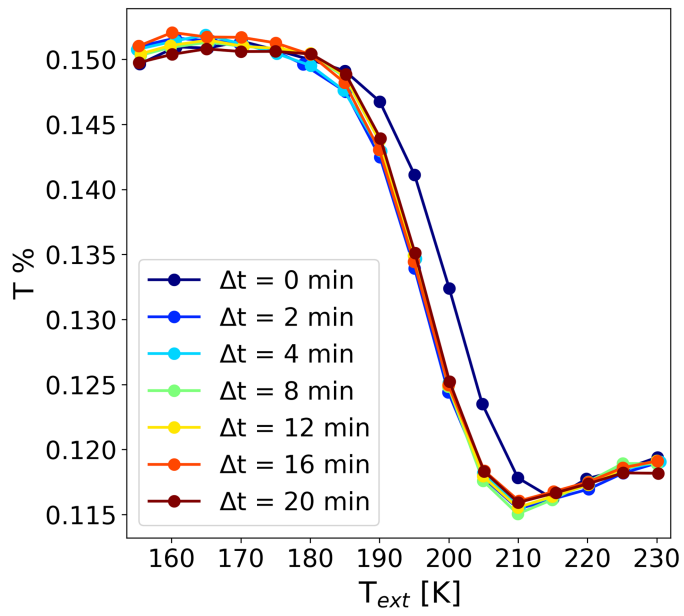
Extended Data Fig. 3 | Dependence of the observed metal-to-insulator phase transition on the waiting time. The temperature evolution of the low frequency transmission (0.2 THz < ω < 1.5 THz) is plotted for different waiting times before starting the THz acquisition.
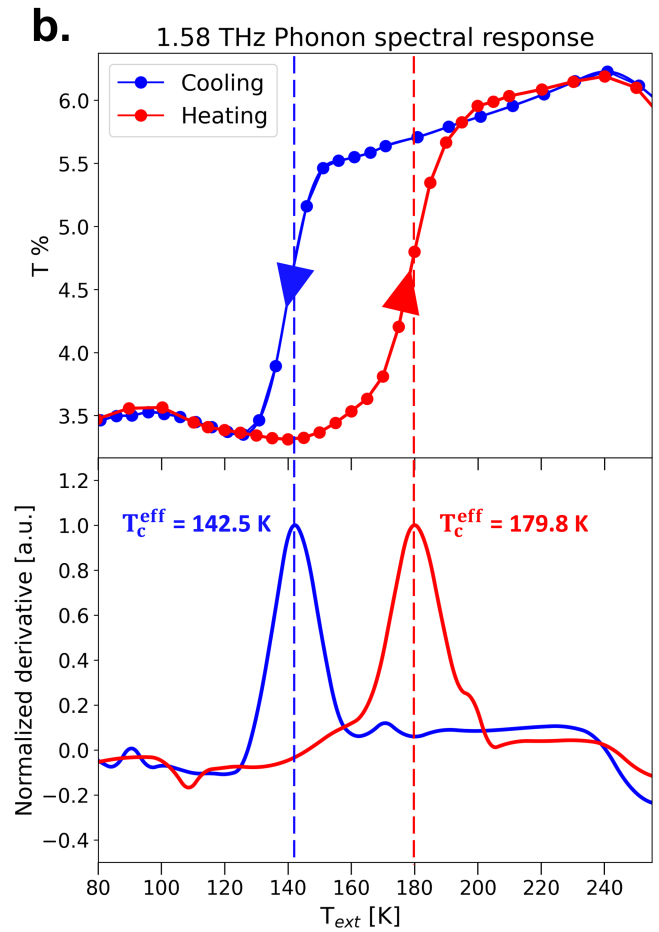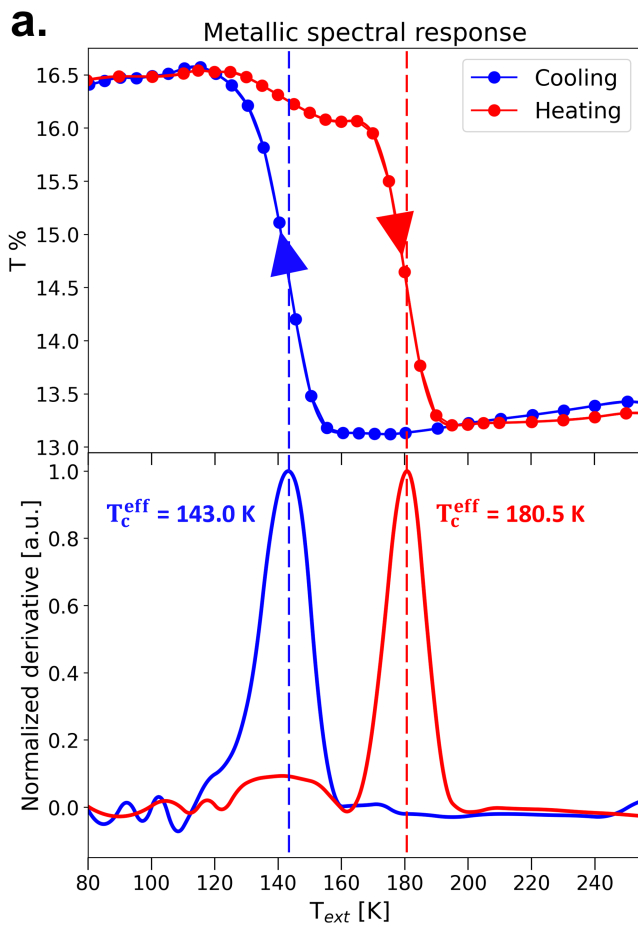
Extended Data Fig. 4 | Determination procedure of the effective critical temperature of the metal-to-insulator transition. a. In the top panel the temperature evolution of the integrated low frequency transmission (0.2 THz < ω < 1.5 THz integration range) upon heating and cooling (circled markers). The solid line is the result of an interpolation. In the lower panel the derivative of the interpolated curve whose maximum sets the effective critical temperature of the phase transition. **b**. In the top panel the temperature evolution of the integrated 1.58 THz phonon transmission (1.53 THz < ω < 1.62 THz integration range) and its interpolation. In the lower panel the derivative of the interpolated phonon response across the phase transition.

a.

b.

c.

d.
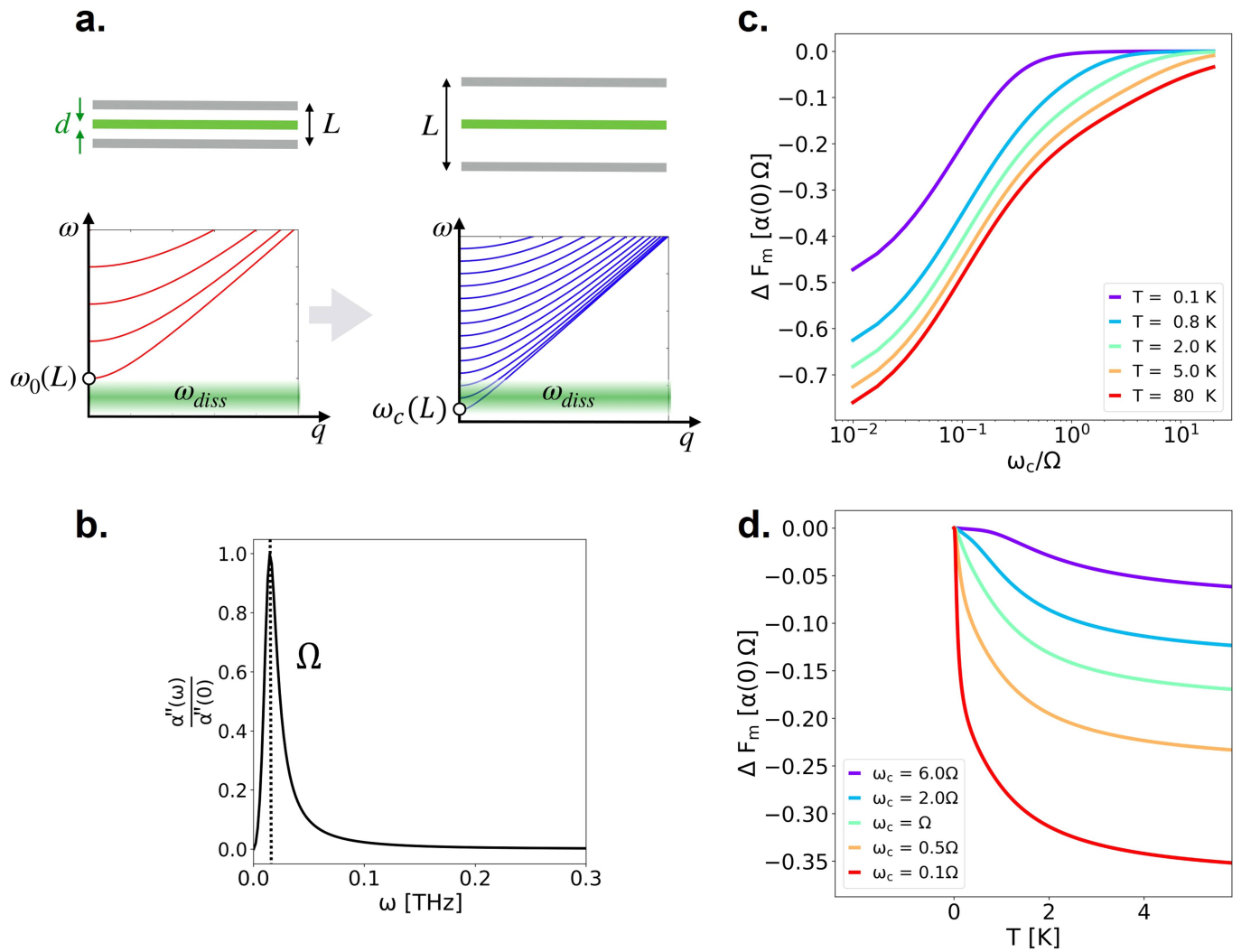
Extended Data Fig. 5 | Cavity-induced renormalization of the free energy of the metallic phase. a. Free energy model setting. Upper panels: coplanar cavity with a thin slab of matter (thickness d) inside a cavity of length L. Lower panels: Sketch of the cavity modes dispersion and of the absorption solid band (green shaded region centered at ω_{diss}). As L is increased, modes are pulled inside and below the absorption band of the solid. The cavity fundamental mode is indicated with $\omega_c(L)$. **b**. Dielectric loss spectrum $\alpha''(\omega)$ ($\Omega = 15$ GHz,

$\gamma = 20$ GHz) employed for the calculations. The spectrum has been normalized by the static contribution to the polarizability $\alpha(0)$. **c**. Renormalization of the metallic free energy ΔF_m as a function of the cavity frequency for different temperatures. The cavity frequencies ω_c are normalized by $\Omega = 15$ GHz. **d**. Renormalization of the metallic free energy ΔF_m as a function of the temperature for different cavity frequencies above and below resonance $\omega_c = \Omega$.
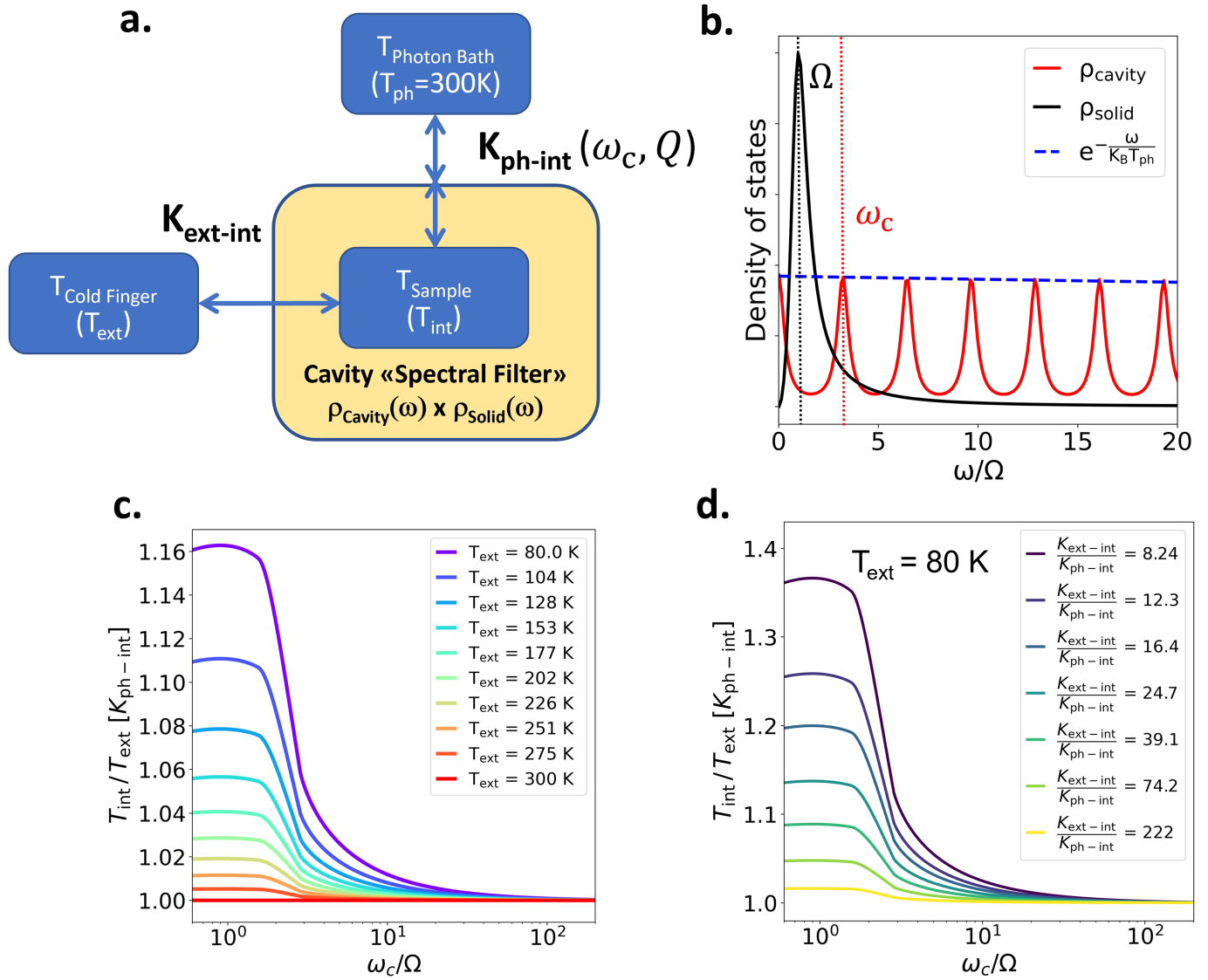
Extended Data Fig. 6 | Cavity control of sample dissipations. a. Schematic representation of the thermal loads on the sample determined by its coupling with the cold finger through the cavity-independent factor $K_{ext-int}$ and with the photon thermal bath through the cavity-dependent factor $K_{ph-int}(\omega_c, Q)$. **b.** Density of states of the solid (peaked at the mode frequency Ω) and of the cavity (peaked at multiples of the fundamental mode ω_c). The cavity density of states is multiplied by the Boltzmann distribution at the temperature of the photon bath $T_{ph} = 300$ K. **c.** Dependence of the temperature ratio $T_{int}(\omega_c, Q)/T_{ext}$ as a function of the cavity frequency for different temperatures of the cold finger T_{ext}. The absolute temperature renormalization scales with $K_{ph-int}(\omega_c, Q)$. **d.** Evolution of the temperature ratio $T_{int}(\omega_c, Q)/T_{ext}$ upon tuning the cavity frequency for different values of the cavity-independent coupling constant $K_{ext-int}$ at a fixed cold finger temperature $T_{ext} = 80$ K. The values of the cavity-independent constant $K_{ext-int}$ indicated in the legend have been normalized by $K_{ph-int}(\omega_c, Q)$ evaluated at $\omega_c = \Omega$.
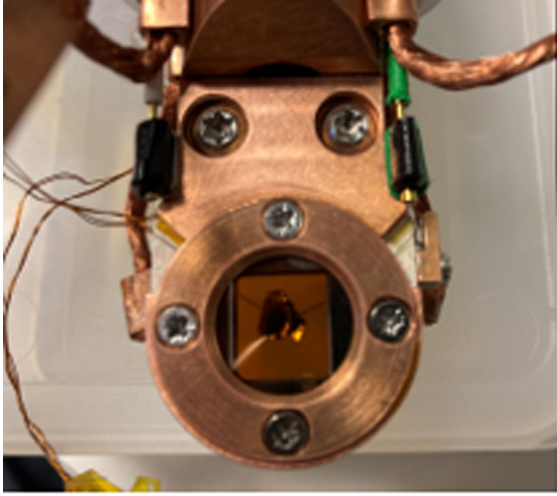
Extended Data Fig. 7 | Temperature measurements set-up. Photograph of the micrometric Cr-Al junction sealed within the membranes and in thermal contact with the sample.
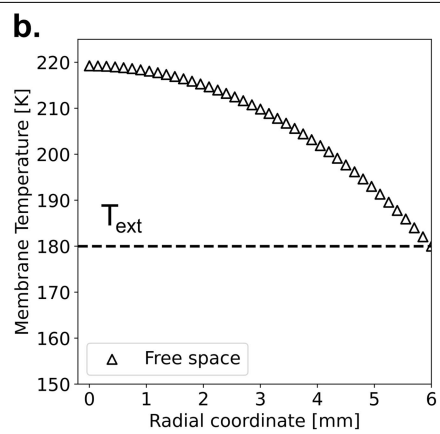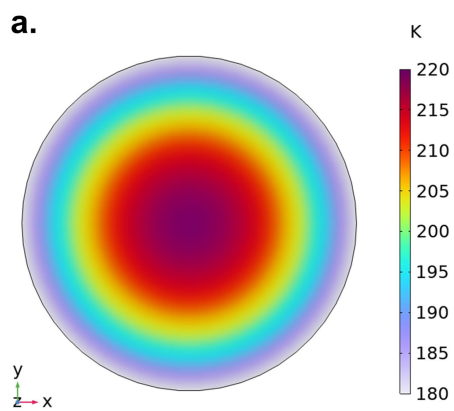
Extended Data Fig. 8 | Finite elements simulation of the membrane's thermal dissipations in free space. a. Simulated 2D temperature profile of the membrane in free space. **b**. Radial dependence of the membrane's temperature held in free space. The cold finger temperature has been set at $T_{ext} = 180$ K.

a.

b.
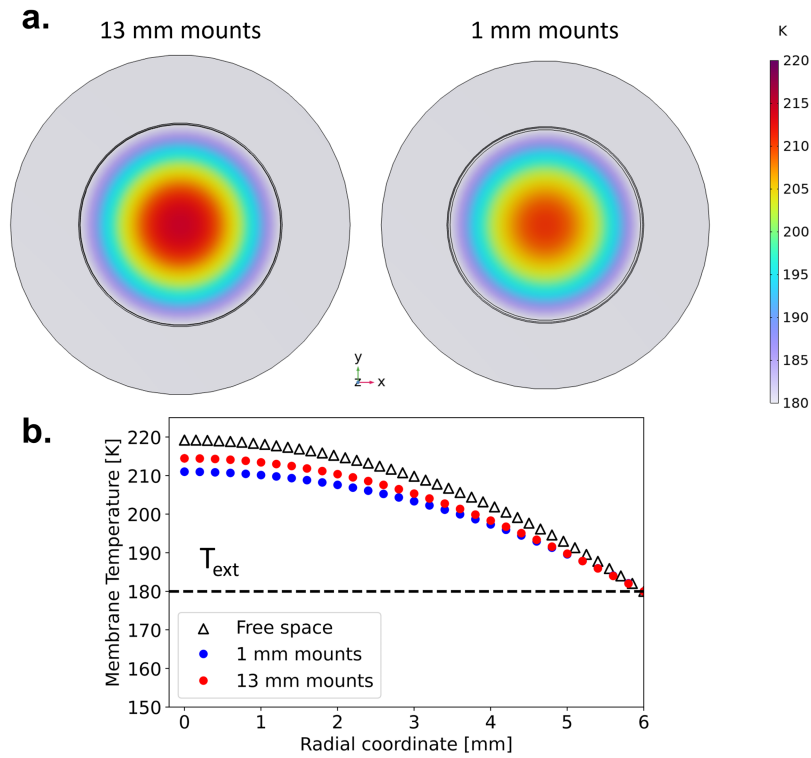
Extended Data Fig. 9 | Finite elements simulation of membrane's temperature as a function of the mirror mounts position. a. 3D thermal profile of the membrane for two representative distances between the mirror mounts (13 mm and 1.0 mm). **b**. Cut of membrane's thermal profile along the radial direction for the two mounts distances presented in a. The cold finger temperature has been set at $T_{ext} = 180$ K, as well as the mounts temperature.